Chem

CellPress

Article

Elucidating the role of cathode identity: Voltage-dependent reversibility of anode-free batteries

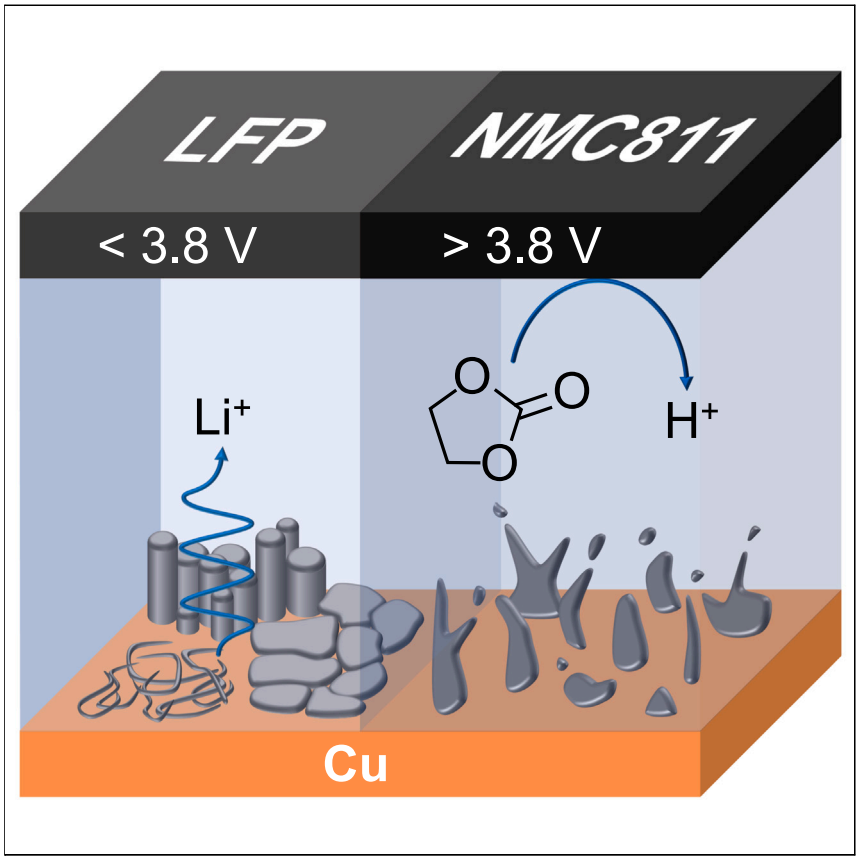

The choice of cathode material for Li metal battery has a multimodal influence on battery degradation, making it inherently challenging to study. Here, we study the impact of operating voltage, as defined by cathode material choice, on cell degradation. We use *operando* NMR to probe Li capacity losses to dead Li and SEI during cycling and attribute the inefficiencies found in NMC811/Cu cells to high-voltage degradation mechanisms in the electrolyte that are not accessible in LFP/Cu.

Yongbeom Kwon, Asya Svirinovsky-Arbeli, Julia C. Hestenes, ..., Piotr Lepucki, Oliver Pecher, Lauren E. Marbella

lem2221@columbia.edu

Highlights

Li metal batteries that use NMC811 deliver lower CE than those that use LFP

Operando NMR enables noninvasive detection of dead Li^0 and SEI

NMC811 cells develop tortuous Li^0 deposits and acids in the electrolyte

SEI formation and corrosion dominate losses in LFP cells

Kwon et al., Chem *10*, 3159–3183
October 10, 2024
https://doi.org/10.1016/j.chempr.2024.06.008

Chem

CellPress

Article

Elucidating the role of cathode identity: Voltage-dependent reversibility of anode-free batteries

Yongbeom Kwon,[1] Asya Svirinovsky-Arbeli,[1] Julia C. Hestenes,[2] Pablo J. Buitrago Botero,[1] Kaitlin Rae M. Corpus,[3] Piotr Lepucki,[4] Oliver Pecher,[4] and Lauren E. Marbella[1,5,*]

SUMMARY

The cathode material in a lithium (Li) battery determines the system cost, energy density, and thermal stability. In anode-free batteries, the cathode also serves as the source of Li for electrodeposition, thus impacting the reversibility of plating and stripping. Here, we show that the reason $LiNi_{0.8}Mn_{0.1}Co_{0.1}O_2$ (NMC811) cathodes deliver lower Coulombic efficiencies than $LiFePO_4$ (LFP) is the formation of tortuous Li deposits, acidic species in the electrolyte, and accumulation of "dead" Li^0. Batteries containing an LFP cathode generate dense Li deposits that can be reversibly stripped, but Li is lost to the solid electrolyte interphase (SEI) and corrosion according to *operando* ^{7}Li NMR, which seemingly "revives" dead Li^0. X-ray photoelectron spectroscopy (XPS) and *in situ* $^{19}F/^1H$ NMR indicate that these differences arise because upper cutoff voltage alters electrolyte decomposition, where low-voltage LFP cells prevent anodic decomposition, ultimately mitigating the formation of protic species that proliferate upon charging NMC811.

INTRODUCTION

Energy-dense batteries are key for electrified transportation, including passenger vehicles,[1,2] heavy-duty automotives,[3–5] and small aircrafts.[6,7] Batteries that contain a lithium (Li) metal anode offer the highest energy density possible for Li-based chemistry. Li metal batteries can contain either a thin (~20 μm) Li metal anode or create a Li metal anode *in situ* using the "anode-free" configuration.[8–11] In an anode-free battery, Li inventory is stored on the cathode side of the battery at fabrication (e.g., layered $LiNi_xMn_yCo_zO_2$ [NMC*xyz*], olivine $LiFePO_4$ [LFP], spinel $Li_{2-x}M_2O_4$) and electrodeposited on a Cu current collector during the first charge step. During discharge, the Li metal anode electrochemically dissolves and the cathode is relithiated. Complete elimination of the Li anode, which is difficult to process and store, presents a major manufacturing, cost, and weight advantage for anode-free batteries compared with systems that come pre-assembled with a thin Li foil.

However, Li metal batteries have been plagued with challenges surrounding Li filament growth that leads to short circuiting and low Coulombic efficiency (CE).[12–22] Over the past decade, advanced electrolyte engineering has discovered several liquid formulations that offer CEs of >99% for Li metal anodes.[23–28] In most of these approaches, additives and/or solvation structures are used to tune the lowest unoccupied molecular orbital (LUMO) of electrolyte components, with respect to the chemical potential of Li, ultimately influencing the composition and the structure of the solid electrolyte interphase (SEI).[20,29–34] A recurring theme in the literature on

THE BIGGER PICTURE

Battery innovation addresses energy storage from renewables and widespread adoption of electrified transportation. In Li-ion batteries, the positive electrode determines the system cost, energy, and safety. When moving from graphite anodes used in Li-ion batteries to Li metal anodes in Li metal batteries, the positive electrode also affects Li metal deposition behavior and the resulting efficiency. In this study, we show that cathodes with different operating voltages undergo different electrolyte reactions that alter Li deposition at the anode. Although enabling higher energies, higher-voltage cathodes lead to lower efficiencies without high pressure, surface engineering, or special electrolytes. In contrast, lower-voltage cathodes enable reversible Li plating under conditions already used for Li-ion batteries. Results from this work provide insights from which one may select battery materials (electrodes and electrolytes) suitable for the desired application (high energy and low cost).

highly optimized electrolytes is that shifting to an anion-derived SEI (e.g., fluorine rich) rather than a solvent-based SEI is beneficial to Li metal battery performance.[26,27,35–42]

Although these design principles are extremely promising for the future of Li metal, most of this testing has been carried out in Li/Li or Li/Cu cells with no cathode present. In principle, the electrodeposition of Li should be independent of cathode choice, but certain cathode degradation reactions are known to impact the anode SEI.[43–46] For example, transition metal dissolution from layered transition metal oxides or spinel cathodes can lead to metal implantation in the anode SEI. Mn in the SEI has been reported to be particularly sinister, where it can increase the permeability of the SEI and lead to continuous electrolyte breakdown.[45,47,48] In addition, electrolyte oxidation and decomposition reactions are exacerbated at high voltage,[49–52] generating species that travel to the anode and contaminate the SEI on Li metal. This adulteration potentially results in a more heterogeneous SEI, leading to nonuniform Li flux during electrodeposition and, in turn, causing lower CE.[53,54]

In this work, we use *operando* ^{7}Li nuclear magnetic resonance (NMR) spectroscopy, post-mortem scanning electron microscopy (SEM), and three-electrode galvanostatic cycling measurements to compare Li electrodeposition from high-voltage NMC811 to low-voltage LFP cathodes. Electrochemical testing indicates that NMC811/Cu pouch cells consistently perform worse than LFP/Cu cells at a range of stack pressures when cycled in conventional carbonate electrolytes. Three-electrode coin cell measurements show that NMC811 cells suffer from severe mass transport issues at the anode, whereas Li nucleation and electrodeposition from LFP is more reversible during battery cycling. We use *operando* ^{7}Li NMR of multilayer batteries to show that these differences are due to tortuous Li deposits generated from NMC811 cathodes that eventually accumulate large quantities of electrochemically inactive Li^{0}, limiting Li^{+} transport to the Cu surface during plating. The electrochemical and chemical decomposition products formed upon charging NMC811 beyond 3.5 V impede Li reversibility, requiring separate solutions for energy-dense Li metal batteries that involve stabilizing the Ni-rich cathode surface. In contrast, Li losses in the LFP/Cu cells are dominated by trace electrolyte impurities, reductive processes at the negative electrode, and corrosion, indicating that electrolyte engineering approaches developed for Li/Cu cells can likely be applied to LFP systems. With more reversible systems where cathode degradation is less of a concern, stabilizing the Li and Cu surfaces will be critical to achieving high CE.

RESULTS

Electrochemical characterization of NMC811/Cu and LFP/Cu batteries

Galvanostatic cycling of NMC811/Cu and LFP/Cu pouch cells reveals that LFP cathodes consistently exhibit higher CE in conventional carbonate electrolyte (1 M $LiPF_6$ in ethylene carbonate/dimethyl carbonate [EC/DMC, 1:1 v/v], LP30). When no external stack pressure is applied, 200 mAh NMC811/Cu pouch cells have an average CE of 78.6% $\pm$ 2.6% (for cycles 1–9), which can be increased to 86.6% $\pm$ 0.1% simply by switching to an LFP cathode (supplemental information, Tables S1, S2, and S5). (Note that we examined the first nine cycles for direct comparison with *operando* experiments, *vide infra*.) This trend persists when the stack pressure is increased to 0.3 MPa and 1.0 MPa, where the average CE over nine cycles of NMC811 cells is 81.3% $\pm$ 4.5% and 94.7% $\pm$ 0.1% compared with 87.4% $\pm$ 0.7% and 95.8% $\pm$ 0.3% for the LFP cells. Differences in the native surface chemistry of the Cu current collectors from the two cell types, made by the same manufacturer,

[1]Department of Chemical Engineering, Columbia University, New York, NY 10027, USA

[2]Program of Materials Science and Engineering, Department of Applied Physics and Applied Mathematics, Columbia University, New York, NY 10027, USA

[3]Department of Chemical and Biomolecular Engineering, UC Berkeley, Berkeley, CA 94720, USA

[4]ePROBE GmbH, Erfurt 99092, Germany

[5]Lead contact

*Correspondence: lem2221@columbia.edu

https://doi.org/10.1016/j.chempr.2024.06.008

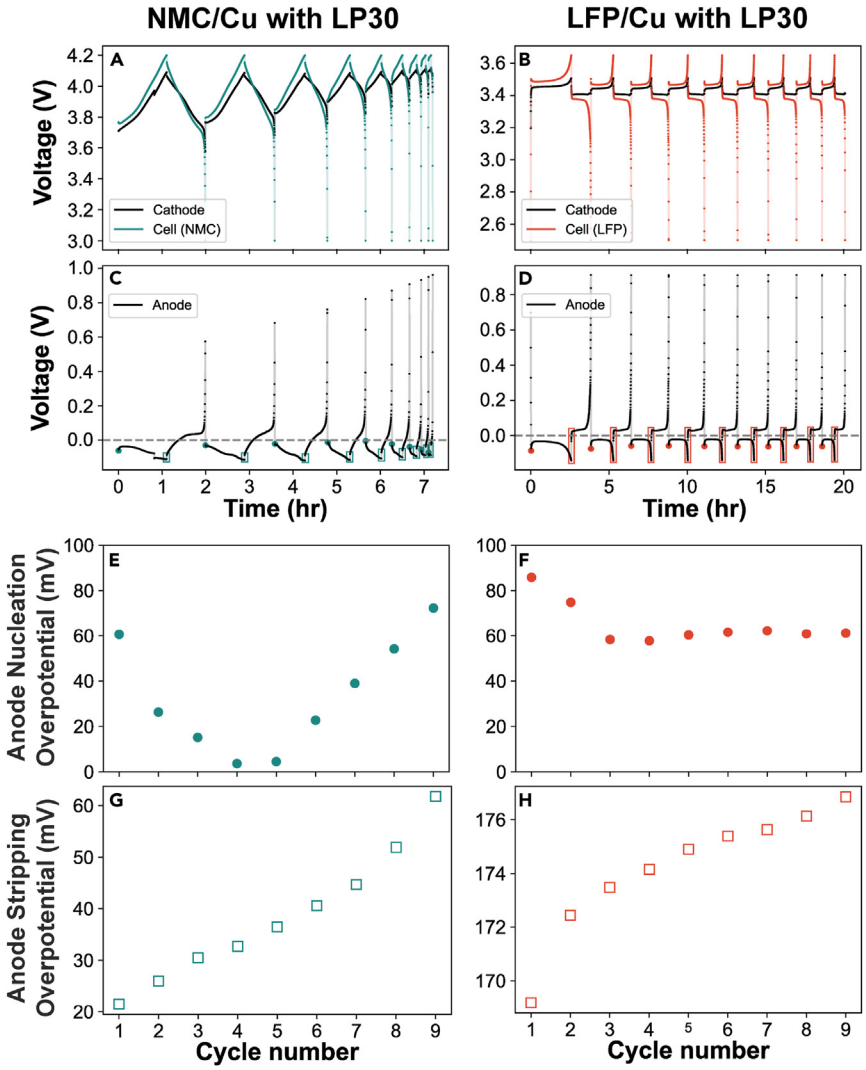

Figure 1. Evaluation of Li electrodeposition from NMC811 and LFP from three-electrode galvanostatic cycling

Voltage profiles of the working electrode (cathode) and total cell voltage in (A) NMC811 or (B) LFP cells, and those of the respective Cu counter electrode (anode) (C and D) from three-electrode measurements during galvanostatic cycling. The anode nucleation overpotential for (E) NMC811 and (F) LFP are measured as the absolute value of counter electrode voltage at the beginning of charge (depicted as colored circles in C and D, respectively), and the anode stripping overpotential for (G) NMC811 and (H) LFP are measured as the voltage increase at the beginning of charge (shown as rectangles in C and D, respectively).

could not immediately account for the discrepancies in battery performance (see Figures S1 and S2; Table S3 for X-ray photoelectron spectroscopy [XPS] data). Metallic Cu, CuO, and small quantities of $Cu(OH)_2$ were detected on both sides of the Cu foil extracted from the as-received pouch cells.

Next, we conducted three-electrode galvanostatic cycling experiments to understand how Li electrodeposition and dissolution varies in NMC811 vs. LFP cells. In the three-electrode setup, Cu is the counter electrode, NMC811 or LFP is the working electrode, and Li metal is the reference electrode. Although most of the cell potential comes from the potential of the working electrode in both NMC811 and LFP cells (Figures 1A and 1B), the voltage profile of the counter electrode is markedly different in each cell type (Figures 1C and 1D).

At the onset of charge for the NMC811/Cu cell, the counter electrode voltage immediately drops upon Li nucleation onto Cu to approximately −0.06 V vs. Li/Li$^+$, which leads to a slight uptick in the overall cell voltage (Figure 1C). Figure 1E shows the absolute value of the Cu counter electrode voltage at the beginning of each plating step. This value represents the overpotential associated with Li nucleation for each individual cycle.[55] After the initial Li nucleation event on Cu, the counter electrode voltage rises to flatten at approximately −0.03 mV (Figure 1C), which is the overpotential associated with the continued growth of Li electrodeposits.[55] However, by $t \approx 0.25$ h, the voltage begins to drop to more negative potentials, suggesting that the system is suffering from mass transport limitations during Li plating.[13] At t = 0.82 h, there is a slight drop in working electrode voltage and a simultaneous uptick in counter electrode voltage, which could indicate a short circuit that is not visible in the electrochemistry of the full cell (Figures 1A and 1C). Nevertheless, the cell continues to charge. At the end of plating, the potential on the counter electrode of the battery dips to approximately −0.11 V vs. Li/Li$^+$, while the full cell reaches a voltage of 4.2 V; these values remain constant in subsequent cycles (Figures 1A and 1C). The upper cutoff voltage of the NMC811 working electrode is relatively steady, rising only 0.02 V between the first (4.09 V) and ninth (4.11 V) cycle.

The absolute value of Li nucleation overpotential with continued cycling decreases from 60 mV in cycle 1 to nearly 0 mV in cycle 4 (Figure 1E). These data suggest that the barrier to forming the Li anode *in situ* is lower when Li can nucleate on preexisting Li metal leftover from the previous cycle, as opposed to the first charge where Li must nucleate onto bare Cu. Another factor for the low energy barrier could be the increasing amount of more favorable nucleation sites, potentially indicating the growth of dendrites where Li can preferentially plate at the tips. By cycle 5, however, there is an inflection point where the decreasing trend of nucleation overpotential flips and starts to linearly increase over the following cycles and the cell exhibits major capacity loss (Figure 1E). Recall that we also suspect that there are mass transport issues involved with Li plating from NMC811. We believe that about halfway through cycling, a highly tortuous environment has developed from porous Li deposits, dead Li, and SEI growth (all of which increase the energy barrier to nucleation), ultimately leading to a substantial drop in capacity by the end of the experiment.

When plating Li onto Cu in the LFP/Cu cell, we see a clear spike in counter electrode voltage at the start of the first cycle that corresponds to nucleation on the Cu current collector at −0.09 V vs. Li/Li$^+$ (Figure 1D). Afterwards, during constant charging, we see the growth of Li deposits with a very low overpotential that ranges from −0.03 to −0.02 V over the course of electrochemical cycling. This low and constant overpotential for Li growth leads to much smaller polarization between the cell and the cathode compared with NMC811, and the cell does not appear to display any major transport limitations. In subsequent cycles, the nucleation overpotential dips and stabilizes to 60 mV by cycle 3 and stays consistent at this value, varying no more than 5 mV, indicating that the barrier for Li electrodeposition remains stable when LFP is the working electrode (Figure 1F).

Likewise, we also measure the stripping overpotential via the instantaneous uptick in counter electrode voltage upon changing polarization from charging to discharging the cell (Figures 1C, 1D, 1G, and 1H). For the NMC811/Cu battery, the stripping overpotential monotonically increases at every cycle. Starting at 22 mV at cycle 1, the energy barrier continues to rise until cycle 9, where the stripping overpotential reaches 62 mV (Figure 1G). Conversely, the stripping overpotential in the LFP/Cu

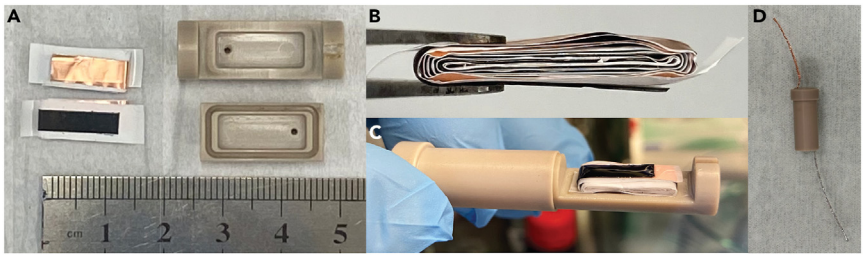

Figure 2. Multilayer *operando* NMR cells

(A) Individual components and dimensions of a dry pouch cell after cutting and winding, and the empty plastic cell capsule sample holder used for *operando* NMR measurements.

(B) Side-view of the nine-layer, prismatically rolled cell that comprises an ~25-mAh anode-free battery.

(C) Nine-layer cell in the PEEK casing for *operando* NMR measurements, when it is fully assembled for *operando* NMR prior to attaching electrochemical leads and sealing.

(D) Sealed *operando* NMR cell showing the Cu and Al mesh that are wound into electrochemical leads.

cell initially exhibits a larger value at 170 mV in cycle 1, but it only increases by 7 to 177 mV by cycle 9 (Figure 1H). Although differences in Li^+ diffusion from the substrate likely impact direct comparison of these values, the higher stripping overpotential in LFP/Cu cells may be due to the fact that Li electrodeposits from LFP are more compact and/or require a higher energy to strip from Cu.[55] In any case, the data indicate that Li dissolution is more reversible when the electrodeposits are produced from LFP than NMC811 (overpotential only changes +7 vs. +41 mV, respectively). As a result, we theorize that LFP and NMC811 likely produce distinct Li deposition morphologies, potentially due to changes in the surface chemistry on the electrode that arise from cycling in a different potential range.

Tracking cycle-by-cycle changes in Li metal deposition morphology with *operando* ^{7}Li NMR in NMC811/Cu and LFP/Cu

From here, we used *operando* ^{7}Li NMR to investigate how Li deposition morphology evolves over the course of cycling in NMC811/Cu and LFP/Cu batteries. In these experiments, we fabricated our samples to replicate the prismatic winding found in the as-purchased pouch cells by cutting them open and reusing the material. The cathode, anode, and separator were sectioned into rectangular strips and re-rolled to form multilayer cells (nine layers in total) that fit into plastic cell capsules (Figure 2) for *operando* NMR measurements in a standard 11-mm solenoid coil. Constructing the smaller multilayer battery produced cells with capacities of approximately 25 mAh from the original 200-mAh pouch. Figure 2A shows the cell dimensions as well as the Cu current collector where a Cu mesh was attached and the black cathode material where an Al mesh was attached and wound into wires for the electrochemical experiment (Figure 2D). The prismatic, jelly-roll cell shown in Figure 2B that was used in *operando* ^{7}Li NMR measurements looks the same as the interior of as-received Li-FUN pouch cells imaged with computed tomography (CT).[56]

With our *operando* NMR cell in hand, we first evaluated the electrochemical performance of the reconstructed nine-layer NMC811/Cu and LFP/Cu cells. In both cases, the LFP cell showed higher CE compared NMC811 over the course of nine charge/discharge cycles (93.8 $\pm$ 3.3 vs. 88.5 $\pm$ 7.6 averaged over two cells; "cell 2" in Tables S4 and S5 was used to evaluate Li deposition morphologies), which is consistent with the performance observed for the as-received pouch cells cycled outside of the magnet at multiple stack pressures (*vide supra*, Tables S1, S2, and S5). Normalized cycle-by-cycle discharge capacity also indicated that our *operando* NMR cells

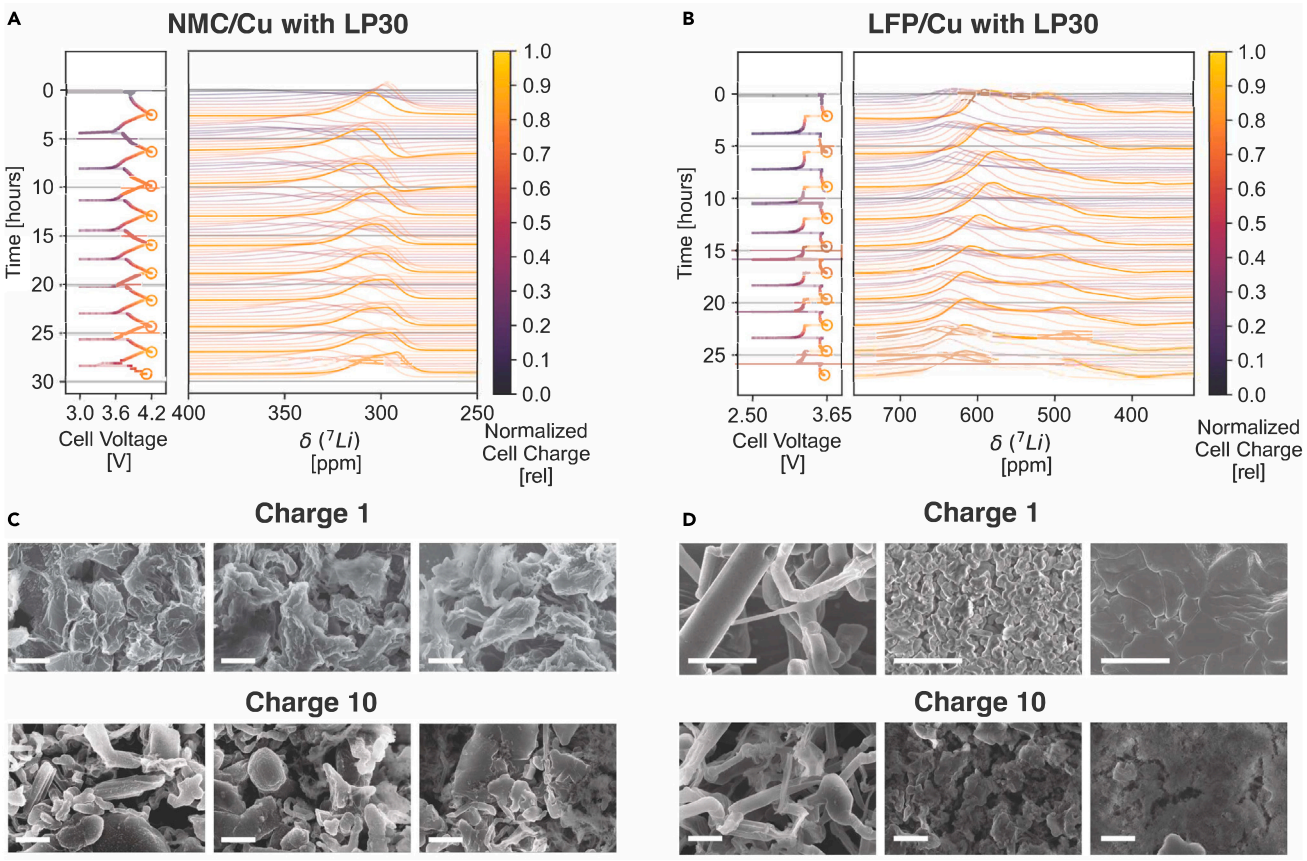

Figure 3. Evolution of Li deposition morphology from NMC811 and LFP during electrochemical cycling

Select *operando* ^{7}Li NMR spectra of (A) the NMC811/Cu cell and (B) the LFP/Cu cell oriented perpendicular (90°) relative to B_0 showing the metallic ^{7}Li resonance alongside the corresponding voltage profiles. Upper cutoff voltage points are circled in orange and the associated NMR spectra are also shown in orange (while the rest of the spectra are faded). Both the NMC811 and LFP cells shown here correspond to those labeled "cell 2" in Tables S4 and S5 that contain their CE values and their discharge capacities extracted from the voltage profiles. SEM images of Li deposition morphologies found in (C) the NMC811/Cu cell and (D) the LFP/Cu cell after one cycle and ten cycles. Scale bars, 2 μm in all images.

had retained their performance after reconstruction from dismantled pouch cells (Table S5). From this comparison, we are confident that the chemical and morphological changes observed in *operando* NMR are representative of practical batteries.

In Figure 3, we show that *operando* ^{7}Li NMR can be used to track the evolution of Li deposition morphology in anode-free multilayer cells with high fidelity during device operation. To achieve a detailed readout of Li plating structures, we take advantage of the orientation-dependent bulk magnetic susceptibility (BMS) effect for planar Li metal deposits vs. high surface area growths[57–61] (Figures 3A and 3B highlight the ^{7}Li metal region of the spectra to see these changes, full spectra can be found in Figures S3A and S3B). When we start the *operando* NMR experiment, the electrode stack is oriented perpendicular to the external magnetic field (90° with respect to B_0) because this orientation has been shown to lead to the highest resolution between dense/planar Li deposits and high surface area Li filaments/needles that grow toward the cathode.[60,62] Due to BMS, flat Li deposits that accumulate on the Cu current collector will be perpendicular to B_0 like the electrodes and appear at lower frequency (i.e., lower ppm values on the x axis in Figure 3). In contrast, high surface area, filament-like structures that grow from the surface of the electrode are oriented parallel with B_0, which shifts their frequency to higher ppm values. Control

experiments using multilayer LFP/Cu and NMC/Cu cells in a z stack configuration (i.e., where the electrodes are stacked rather than wound) indicate that BMS effects from Li plating on the folded region (which only contributes to ~5% of the total ^{7}Li NMR signal) does not change the spectral interpretation below (see Figures S6 and S7 and the supplemental information for more details).

In Figures 3A and 3B, we highlight the end of Li plating (cell charging) in each cycle with an orange circle to denote the upper cutoff voltage for each cell type (for NMC811, this upper cutoff voltage is 4.2 V; for LFP, it is 3.65 V). During the initial charging event in the NMC811/Cu cell, we see that this time point also corresponds to an orange ^{7}Li NMR spectra, where an intense Li metal peak has grown in with a shift at 298 ppm. Close examination of this ^{7}Li metal resonance shows a relatively symmetrical peak shape (slight tail to the left) with a narrow linewidth (fwhm = 2,993 Hz, Figure 3A). The mostly symmetrical NMR line suggests that these deposits are uniform and low surface area. To confirm this spectral interpretation from inside of the cell, we analyzed identical NMC811/Cu plastic cell capsules after a single charge to 4.2 V with post-mortem SEM. The top image in Figure 3C shows that the resulting Li deposits are mossy, with Li metal structures ranging from 2 to 4 μm wide. As the original *operando* NMR cell continues to cycle, we noticed that the ^{7}Li metal resonance develops a clear high frequency shoulder at ~302 ppm that increased the overall linewidth to fwhm = 4,156 Hz, consistent with the formation of Li filaments. Again, we extracted the anodes from separate plastic cell capsules and confirmed that, after ten cycles, NMC811/Cu cells grow high surface area Li filaments (approximately 1 μm in size) that cover the Cu current collector (Figure 3C, bottom). From these data, we gather that NMC811 cathodes initially plate porous, mossy Li deposits on the Cu surface that transition into even higher-surface-area, filament-like structures as cycle number increases. This change in deposition morphology is correlated with a gradual drop in capacity in the electrochemistry, with an average CE value of 92.1% (Table S4).

In contrast, the LFP/Cu cells show much more complex peak shapes even after the first charge step (Figure 3B). Some of this line broadening and peak distortion is likely due to the stray field created by BMS because Li metal is in close proximity to multiple layers of LFP (Figure S4), but some is also due to distinct Li deposition morphologies that are formed upon plating Li from LFP. Once the cell is charged to 3.65 V, we see that the ^{7}Li metal resonance shows at least two distinct peaks, one at 509 ppm and another at 589 ppm, with an overall fwhm = 18,125 Hz. Note that in both of the multilayer batteries examined here, we observed higher-than-expected shifts for Li metal (centers of mass at ~300 ppm for NMC811 cells and ~550 ppm for LFP cells) that deviate from the Knight shift, which typically appears between 240–270 ppm.[63] These changes in Li metal Knight shift are attributed to compounding BMS effects from the different cathode compositions (μ_{eff} [NMC811] = 2.1 μ_B[64] and μ_{eff} [LFP] = 4.9 μ_B[65]) and the amount of cathode in the cell (see Figures S4–S9 and additional discussion on BMS effects in the supplemental information). In any case, the fact that the NMR lineshape exhibits both high frequency and low frequency components indicates that a range of Li deposition morphologies is present upon plating Li from LFP. SEM images of the Li deposits formed after the first charge confirm this spectral interpretation, showing a wide range of plated structures, including ~1-μm-thin whisker-like Li filaments, mossy Li growths, and dense Li deposits (Figure 3D, top). At the end of the tenth charge, two distinct peaks remain, but have shifted downfield to 511 and 622 ppm, respectively, increasing the fwhm to 23,387 Hz, indicating that the Li deposits are still heterogeneous but have likely increased in surface area. SEM imaging of the anodes extracted from cells after

ten charge cycles also show heterogeneity in Li deposition morphologies, where several types of microstructures can be found (Figure 3D, bottom). From these observations, we conclude that LFP/Cu cells largely retain an assortment of Li deposition morphologies from charge step one through ten, as opposed to NMC811/Cu cells that transition from mossy microstructures to needle-like growths. We suspect that the dense Li regions produced from LFP are able to strip more effectively, exposing fresh Cu surface after stripping each cycle. This also may explain why the nucleation and stripping overpotentials stay the same cycle-to-cycle in the three-electrode measurement (Figure 2). The more consistent Li stripping/plating behavior in LFP/Cu cells is also reflected in a higher CE value of 93.6% (Table S4).

Quantifying Li loss pathways in NMC811/Cu vs. LFP/Cu cells

To further probe the mechanistic origin underpinning differences in Li plating reversibility between NMC811 and LFP, we can also use *operando* ^{7}Li NMR to quantify individual sources of Li loss. Within this system, we consider two sources of Li loss: (1) electrochemically inactive Li^0 that breaks off from the underlying electrode and is electronically isolated, no longer participating in electrodeposition, i.e., dead Li^0, and (2) Li^+ in the SEI, which encompasses irreversible capacity losses to form the passivation layer on the electrode surface; in our calculations this term also includes any Li lost to corrosion (see below).[59] However, we must first ensure that our NMR measurements are quantitative in nature. Our multilayer battery samples have higher capacity than single-layer cells and therefore contain more Li metal and metal current collector. The extra metal presents challenges for quantitative *operando* NMR due to skin depth effects that attenuate the signal.[59,63,66] Thus, prior to analyzing the source of Li loss, we determined the conditions where we could achieve quantitative accuracy in multilayer systems. The variable tilt angle experiments described in the supplemental information indicate that positioning the cell at the magic angle improves the signal-to-noise ratio of Li metal at the expense of resolving Li metal morphology (Figure S8), so the following measurements were performed with the electrodes at $\alpha = 54.7°$.[62] Nutation experiments on plated Li metal vs. residual Li left behind after the stripping step indicate that near-quantitative NMR can be performed on dead Li^0 (Figure S9) because the microstructures (2–4 μm) are smaller than the skin depth of Li at this field strength (10.7 μm, see the supplemental information for a description of quantification with NMR and error analysis). As a result, dead Li^0 can be used to directly quantify Li losses, together with electrochemical data. These data also suggest that the metal current collectors do not pose a major problem for quantification but, rather, only the dense Li deposits formed upon plating with thicknesses greater than the skin depth. In order to calculate the quantity of dead Li^0 in the cell at each cycle from the NMR signal intensity, we constructed an external calibration curve using serially diluted samples of LP30 (Figure S10). This calibration curve allows direct conversion of integrated ^{7}Li NMR signal for dead Li^0 (in the metallic region) to the mass of Li. Then, the mass of Li^0 (in mg) is converted to the capacity loss associated with inactive Li^0 ($Q_{Li,dead}$, units of mAh) using Faraday's first law of electrolysis. The amount of Li^+ irreversibly trapped in the SEI ($Q_{Li,SEI}$) is then calculated by subtracting $Q_{Li,dead}$ from the irreversible capacity loss from the electrochemical data (Q_{irr}) as follows:

$$Q_{Li,SEI} = Q_{irr} - Q_{Li,dead} \quad \text{(Equation 1)}$$

Figure 4 shows the *operando* ^{7}Li NMR spectra used to quantify the capacity lost to dead Li^0 and Li in the SEI in NMC811/Cu and LFP/Cu cells (full spectra can be found in Figures S3C and S3D). Even though we cannot be quantitative regarding the amount of Li metal deposited on the Cu substrate at full charge, a qualitative comparison of plated Li vs. stripped Li indicates that Li deposition/dissolution from LFP is

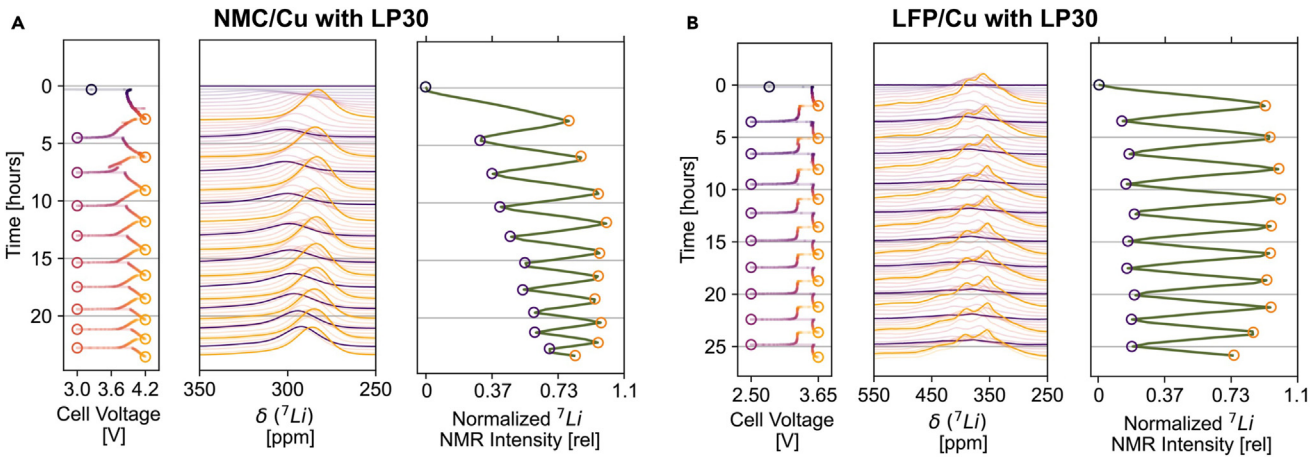

Figure 4. Quantification of Li deposition and dissolution in NMC811/Cu and LFP/Cu cells during electrochemical cycling

Operando ^{7}Li NMR spectra of (A) NMC811/Cu and (B) LFP/Cu, with LP30 oriented at the magic angle (54.7°) relative to B_0, showing the metallic ^{7}Li resonance alongside the corresponding voltage profiles. Upper and lower cutoff voltage points are circled in orange and purple, respectively, with the associated NMR spectra shown in the middle of each panel. The right panel shows the integrated ^{7}Li NMR signal intensity for Li at the end of plating (orange) and residual inactive Li^0 left on Cu after stripping (purple). Both the NMC811 and LFP cells shown here correspond to those labeled "cell 1" in Tables S4 and S5 that contain their CE values and their discharge capacities extracted from the voltage profiles.

highly reversible (third panel, Figure 4B). The lack of dead Li^0 accumulated in the cell after each discharge step is also shown by the constant signal intensity in the purple spectra. In contrast, the NMC811/Cu cell shows a progressive buildup of dead Li on the Cu current collector after stripping (purple spectra, Figure 4A) that represents accumulated capacity loss. Similar to the previous *operando* ^{7}Li NMR measurements, the average CE of NMC811/Cu is lower than that of LFP/Cu (84.9% vs. 93.9%, respectively).

To quantify the amount of Li lost to electrochemical inactive Li^0 in each system, we extract the integrated ^{7}Li NMR signals from Figure 4 that correspond to Li^0 (in the metallic region) at the end of each discharge step and convert this to mass of Li using our external calibration curve (Figure S10). Recall that this is possible because our nutation experiments in Figure S9, discussed above, indicate that the metal particles that make up dead Li^0 are small enough to avoid major skin depth effects (<10.7 μm). With the amount of inactive metallic Li^0 in hand, this value is converted to capacity ($Q_{Li,dead}$) and, using Q_{irr} from our electrochemical measurement, is used to find the capacity lost to Li^+ in the SEI according to Equation 1 (Tables S6 and S7). These numbers were converted to percent capacity loss at each cycle and are plotted in Figure 5 (see supplemental information for further details on calculations). In the first cycle, we see that both cells (NMC811/Cu and LFP/Cu) show lower CE compared with subsequent cycles. In both cases, electrochemically inactive Li^0 accounts for approximately 40% of the Li loss while the remaining 60% is lost to SEI formation (Figures 5C and 5D). In the NMC811/Cu cell, Li^+ in the SEI continues to be the predominant mode of Li loss until cycle six, when the mechanism switches and the amount of inactive Li^0 in the cell grows drastically. After this point, dead Li^0 accounts for nearly all of the loss in the system (Figure 5C). The sustained growth of SEI followed by the sharp accumulation of dead Li^0 is consistent with our *operando* ^{7}Li NMR measurements optimized to detect Li plating morphology, post-mortem SEM, and three-electrode cycling experiments, which all indicated growth of high surface area Li after continued cycling. For instance, during the *operando* ^{7}Li NMR experiment shown in Figure 3, we see the appearance of a high frequency shoulder at about cycle 6 that indicates Li filaments have plated on the Cu current collector

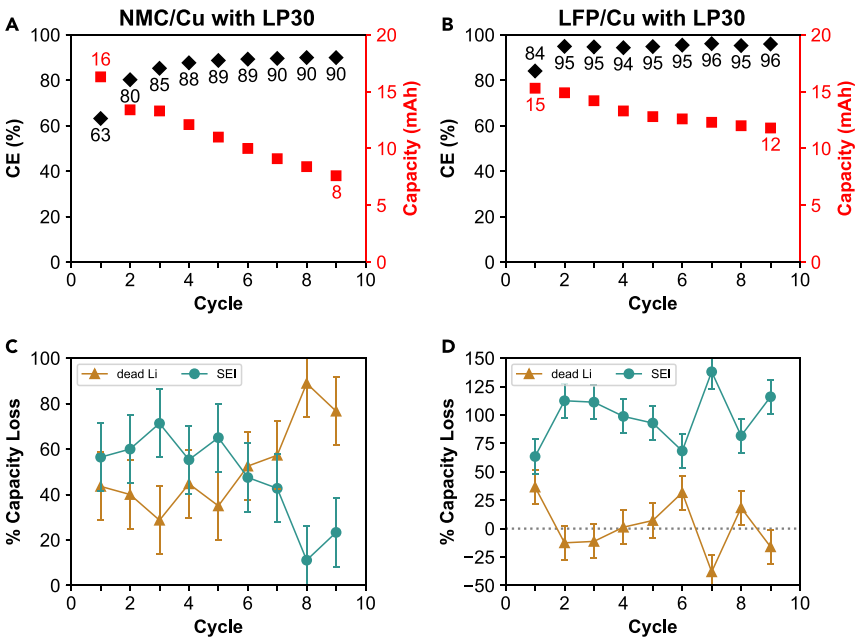

Figure 5. Mechanisms of Li loss in each cycle for NMC/Cu and LFP/Cu cells

(A and B) Cycle-by-cycle CE (black) and discharge capacity values (red) as well as (C and D) % capacity loss to inactive dead Li^0 (orange) and Li^+ in the SEI (green) for (A and C) NMC811/Cu with LP30 and (B and D) LFP/Cu with LP30. Error bars in (C and D) represent a maximum error of 15% from rf signal attenuation in Li metal filaments. The error propagation procedure used to calculate the error bars from the NMR integrals is described in the supplemental information.

(precursory to dead Li^0), also observed in SEM images at cycle 10. As Li ions try to repeatedly plate and strip during cycles 5 to 9, they must make their way through a tortuous network of accumulated dead Li^0, and this process was detected via the sloping voltage profile at the anode in the three-electrode measurement (Figure 1C). Interestingly, although the plastic capsule cells used for *operando* NMR experiments and the three-electrode coin cells have distinct constructions, both experiments showed an inflection point at cycle 5 that coincides with the predominant mode of Li loss (dead Li^0 vs. SEI, Figure 5C) and plating overpotential (Figure 1E), respectively. We speculate that there is a correlation between these disparate signs of battery degradation, where it switches from being an SEI-dominant to an inactive Li^0-dominant loss mechanism. We are conducting more experiments to collect additional statistics to test this hypothesis.

Even though Li losses are nearly identical between the NMC811/Cu cell and the LFP/Cu cell in cycle one, almost all subsequent losses in the LFP/Cu system are due to surface reactions (Figure 5D). In fact, many individual cycles in LFP/Cu show negative values when capacity is lost to inactive Li^0, indicating that Li atoms that are lost to electrochemically inactive Li^0 on the previous cycle are somehow "revived" on the next cycle. Although it is difficult to definitively discern which mechanisms may be at play, the apparent recovery of inactive Li^0 seen in Figure 5D is consistent with galvanic corrosion and/or soft shorting.[59,67]

During galvanic corrosion, residual Li metal in contact with the Cu anode forms a galvanic pair and is oxidized to Li^+ ($Li^0 \rightarrow Li^+ + e^-$), and thus this process would contribute to the next electrochemical cycle and lead to a loss in ^{7}Li metal NMR signal intensity (these Li atoms would then be counted in the $Q_{Li,SEI}$ term in

Equation 1). The rates at which corrosion occur in cells with NMC811 or LFP cathodes were investigated by cycling for 10 charge/discharge cycles, followed by leaving the cell (discharged) in the magnet at open circuit voltage while recording the ^{7}Li metal NMR signal intensity decay.[59] In this experiment, we found that the LFP/Cu cells had much higher rates of corrosion when compared with NMC811/Cu, even reducing the ^{7}Li metal NMR signal intensity by 90% of the original signal strength after 25 h (Figure S11). This is a surprising finding, as it suggests that some of the residual Li, above defined as dead Li^{0}, is partially electronically connected to the Cu allowing the charge transfer. These Li deposits were likely left over due to stripping overpotential or cathode lithiation overpotential that prevented a complete discharge to the lower cutoff voltage. Furthermore, the electron passed from Li oxidation to the Cu travels to a bare Cu surface in contact with electrolyte and ultimately results in electrolyte reduction.[68] This indicates that there is a greater surface area of bare Cu, exposed from clean stripping of Li metal upon discharging the LFP/Cu cell compared with NMC811/Cu. Indeed, we can visually observe more bare Cu surfaces after stripping in LFP cells vs. NMC811 cells (Figure S12). Compared with the LFP cell, NMC811/Cu batteries showed a much slower corrosion rate in *operando* ^{7}Li NMR, with the ^{7}Li resonance decreasing only 17% over the course of 45 h. This observation suggests that residual dead Li^{0} is not electronically connected to the Cu and is likely surrounded by a thicker SEI layer, consistent with the tortuosity argument presented above. We note that this analysis neglects chemical reactions between residual Li^{0} and the electrolyte, which can diffuse through preexisting passivation layers, and this mechanism likely accounts for some of the decrease in NMR signal intensity in both cells (thus overestimating corrosion rates). Nevertheless, these measurements indicate that corrosion and parasitic reactions occur on the order of tens of hours, allowing us to accurately quantify all of the Li^{0} remaining at the end of any cycle.

In an electrochemical shorting event, Li^{0} filaments dissolve and return to Li^{+}, which would cause similar changes in ^{7}Li NMR signal intensities. A closer examination of the voltage profiles for the anode in Figure 1 show that they are squared off with a low overpotential, which may hint that soft shorting is at play as the Li deposits become more needle-like (Figure 3).[67] However, this is by no means a definitive diagnosis for shorting in these cells. In any case, the LFP cell clearly does not suffer from a massive buildup of dead Li^{0} like the NMC811/Cu system; rather, most of the capacity loss can be attributed to parasitic side reactions, galvanic corrosion, and/or soft shorting. The capacity loss when Li is plated from LFP may be due to the fact that the system primarily relies on electrochemical reduction products to passivate the Li surface due to the low operating voltage of the cell rather than high-voltage degradation of the electrolyte originating from cathode-side reactions.

Characterizing electrolyte decomposition reactions and Li surface chemistry

Electrolyte reduction as well as chemical crosstalk during the initial Li deposition event will generate an SEI on both the Cu current collector and the growing Li metal surface, which can impact reversibility. Given that NMC811 and LFP have different operating voltages and structures, we expect that changes in electrolyte oxidation pathways may impact the composition and arrangement of the SEI. The presence of different types, or even just different quantities, of electrolyte decomposition products can have a profound impact on Li^{+} flux to/from the Cu current collector and result in distinct Li deposition morphologies as well as stripping efficiencies.

We used post-mortem XPS to characterize the chemical composition of the SEI on Li metal anodes extracted from NMC811/Cu and LFP/Cu pouch cells after 10 cycles

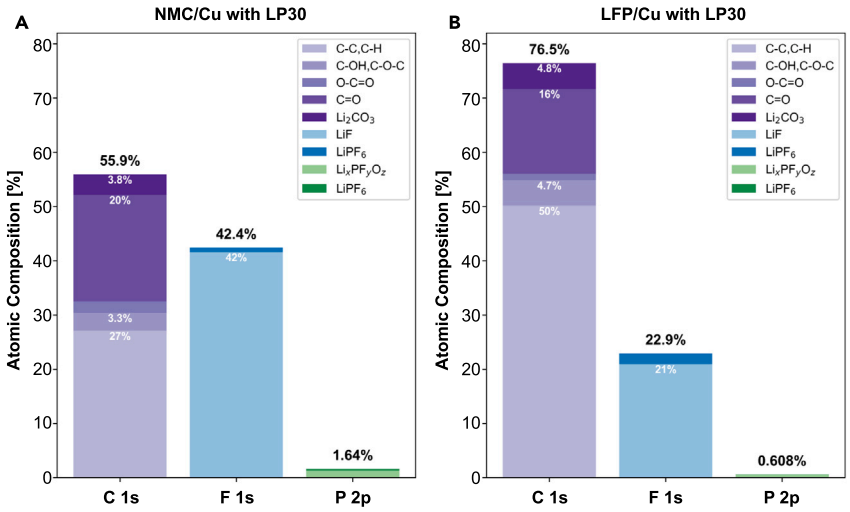

Figure 6. Chemical composition of the Li SEI generated from NMC811 and LFP

Quantification of C 1s (purple), F 1s (blue), and P 2p (green) orbitals from XPS spectra of Li metal anodes extracted from (A) NMC/Cu and (B) LFP/Cu cells in LP30 after ten galvanostatic charge/discharge cycles at C/2.

(after the final stripping step) (Figures 6 and S13). Very little residual electrolyte salt ($LiPF_6$) is seen on the electrode surfaces, likely due to the fact that we wash extracted Li metal anodes with DMC prior to analysis. This procedure removes $LiPF_6$, soluble species of the SEI (like $Li_xPF_yO_z$), and weakly attached components (e.g., even insoluble LiF embedded in organic phases), which would no longer be observed via XPS. Therefore, we assess the relative amounts of different surface phases observed in XPS and evaluate them in the context of our other experiments (e.g., *in situ* NMR, three-electrode cycling data) to understand how electrolyte decomposition and the resulting Li SEI impacts Li cyclability.

The most obvious difference observed in XPS is that Li metal electrodeposits in the NMC811 cell contain higher quantities of LiF (binding energy [BE] = 685.2 eV in F 1s), indicating (1) a possible divergence in $LiPF_6$ breakdown when the upper cutoff voltage is raised beyond 3.65 V and/or (2) alterations in the Li surface from reactions between acidic species in the electrolyte produced at high voltage (e.g., HF) and existing SEI compounds (e.g., Li_2CO_3).[40] The former is consistent with *in situ* NMR experiments, where we directly monitor $LiPF_6$ breakdown pathways during battery operation without cell disassembly (see below). The latter is also supported by the fact that *in situ* NMR of the NMC811 cell produces higher quantities of HF during cycling, which can react with Li_2CO_3 in the SEI to produce more LiF (again, see below). Previous reports indicate that acidic species in the electrolyte can degrade the SEI, making it more porous[40] and also more resistive (e.g., from more LiF), possibly explaining some of the mass transport effects that we see in three-electrode experiments with the NMC811 cathode shown in Figure 1C. In contrast, Li surfaces generated from LFP appear to exhibit higher quantities of organic compounds. This may be due to solvent reduction that occurs during Li plating or the difference in SEI properties (e.g., due to changes in salt decomposition) that allow reaction between Li metal and DMC during sample preparation. In general, we also find that the organics on the NMC811-derived Li surface are more oxygenated (e.g., appear at higher BE in C 1s, Figure S13), consistent with oxidative decomposition at the cathode that is then transferred to the anode.

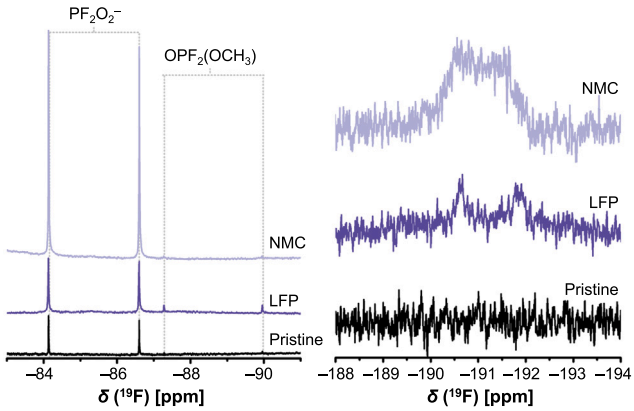

Figure 7. Chemical analysis of degradation products in the electrolyte of NMC811/Cu and LFP/Cu cells after cycling

In situ ^{19}F solution NMR showing the electrolyte decomposition products formed after 10 galvanostatic cycles at C/10 in NMC/Cu (top, light purple) and LFP/Cu (middle, dark purple) compared with the pristine LP30 electrolyte (bottom, black).

The difference in SEI chemistry between NMC811 and LFP cells indicates that high-voltage decomposition processes impact Li plating morphology, subsequently leading to performance decline. Figure 7 shows *in situ* ^{19}F solution NMR depicting the breakdown products of $LiPF_6$ salt for both battery types produced after ten cycles. In the pristine, battery-grade electrolyte, we see a small amount of $PF_2O_2^-$ at $\delta(^{19}F) = -85.2$ ppm ($^1J_{P-F} = 938$ Hz), likely due to the hydrolysis of $LiPF_6$ from trace water (Karl Fischer measurements in our laboratory are below the detection limit <10 ppm). Trace quantities of $OPF_2(OCH_3)$ ($\delta(^{19}F) = -88.5$ ppm, $^1J_{P-F} = 1{,}004$ Hz) are also detected in the pristine electrolyte, possibly resulting from a reaction between the salt and methanol impurities from DMC hydrolysis.[51] Upon cycling both LFP/Cu and NMC811/Cu, we see evidence of $LiPF_6$ decomposition with the appearance of a doublet that corresponds to HF centered at approximately −191.3 ppm ($^1J_{H-F} = 474$ Hz),[69] where more HF is formed upon cycling NMC811 than LFP. Further, we see that the NMC811 cell contains a large amount of $PF_2O_2^-$ after cycling (the signal integral increasing by a factor of 8.1 from the pristine sample), but very few other salt decomposition products. In the presence of LFP, a relatively small amount of $PF_2O_2^-$ is produced (only increasing by a factor of 1.2 from the pristine) along with $OPF_2(OCH_3)$. Given that these species appear in ^{19}F solution NMR, and almost no phosphorus-containing compounds were detected in XPS, we conclude that these components fail to passivate the Li metal surface, as they appear to readily disperse into the electrolyte rather than deposit in the SEI. The different amount of these compounds in NMC811 vs. LFP cells also points to cathode- and voltage-dependent formation mechanisms of acidic salt decomposition products (e.g., HF, PF_5, etc.) that impact the SEI and Li deposition/dissolution processes (see discussion for further details).

DISCUSSION

The combination of electrochemical characterization, XPS, SEM, and ^{7}Li/^{19}F NMR indicates that the choice of cathode material changes the interphase on the opposing electrode surface and thus alters the plating morphology and plating reversibility of Li. To understand how this works, we first consider the composition of the electrolyte at open circuit voltage in both NMC811 and LFP cells. At this stage, both cells contain 1 M $LiPF_6$, a 1:1 ratio of EC:DMC, and trace water that can hydrolyze the electrolyte components in an identical fashion (Scheme 1). In terms of solvents, linear

(1.1) LP30 electrolyte salt and solvent

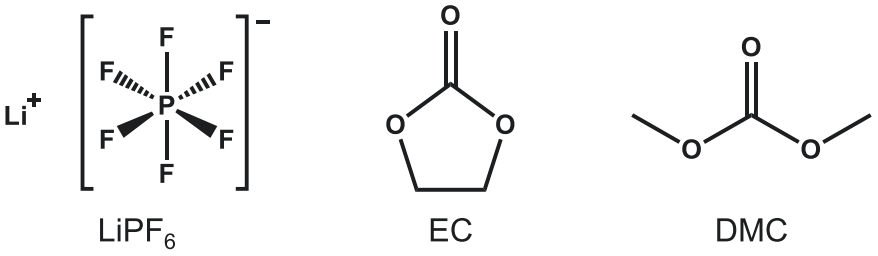

(1.2) Hydrolysis of DMC

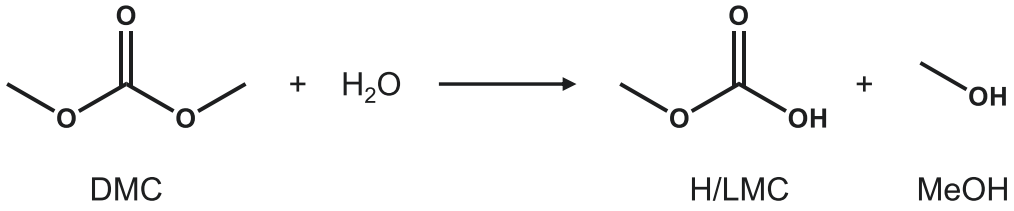

(1.3) Hydrolysis of $LiPF_6$

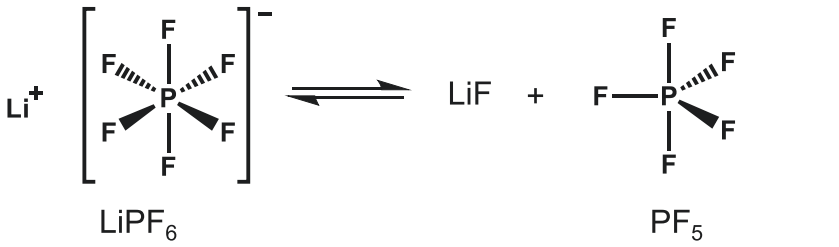

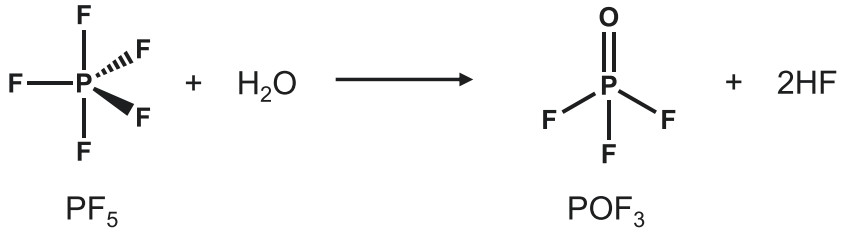

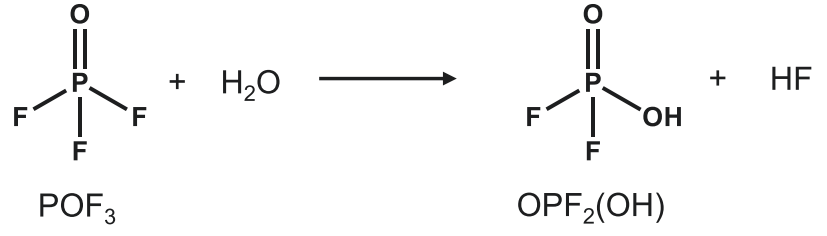

Scheme 1. Proposed electrolyte decomposition reactions that take place in pristine LP30 electrolyte

Electrolyte salt and solvent materials in LP30 (1.1, top), proposed reaction for the hydrolysis of DMC that generates H/Li^+ methyl carbonate and methanol (1.2, middle), and proposed reaction for the hydrolysis of $LiPF_6$ (1.3, bottom).

DMC is more susceptible to hydrolysis, where water can form low quantities of methanol and hydrogen or Li methyl carbonate (H/LMC) prior to cycling.[51] Examination of ^{1}H NMR of the pristine electrolyte indicates that the hydrolysis products of the solvent are below the detection limit and/or have gone on to participate in other reactions (Figure S14); only EC and DMC are observed. If we turn to the ^{19}F NMR shown in Figure 7, we see a small doublet ($\delta(^{19}F) = -88.5$ ppm, $^1J_{P-F} = 1{,}004$ Hz) that corresponds to $OPF_2(OCH_3)$ and that can be produced from $OPF_3 + CH_3OH \rightarrow OPF_2(OCH_3) + HF$, which supports Scheme 1.2. In the ^{19}F NMR, the major hydrolysis product detected is $PF_2O_2^-$, the end-product of $LiPF_6$ hydrolysis together with HF (Scheme 1.3).[70] Analysis of ^{19}F NMR (Figure S15) also shows that the ratio of $PF_2O_2^-$:PF_6^- is 0.00069, which corresponds to a water concentration of approximately 9.8 ppm, according to the stoichiometry in Scheme 1.3. This concentration is consistent with Karl Fisher measurements in our laboratory that are below the detection limit of 10 ppm. Note that HF is not detected in ^{19}F NMR of the pristine electrolyte, likely due to its volatility (b.p. = 19.5°C).

Next, we evaluate the (electro)chemical reactions that occur as both batteries begin to charge by examining oxidative processes and subsequent decomposition reactions at each cathode. Although the processes that occur in the presence of NMC811 have been investigated to some extent, less is known regarding LFP. During charging, both cells reach 3.5 V where trace methanol in the electrolyte is oxidized to formaldehyde,[71] generating protic species according to Scheme 2. These protic species accelerate the decomposition of PF_6^- to form PF_5 and HF, which is observed in ^{19}F NMR (Figure 7). After this point, the cycling conditions of the two cells diverge as the NMC811/Cu cell charges to higher voltages and we ultimately see different end products in solution NMR and in the SEI on Li. Although the upper cutoff voltage of the LFP/Cu cell is set to 3.65 V, three-electrode measurements show that the voltage of the cathode never goes above 3.51 V vs. Li/Li^+ and only small amounts of HF are generated at this potential (Figures 1B and 7). Therefore, we expect that this cell will contain a low concentration of water due to the reaction of Li_2CO_3 with HF to form LiF, CO_2, and H_2O (Scheme 2), which is consistent with the lower amount of LiF seen in XPS for the SEI on Li cycled vs. LFP compared with NMC811 (Figure 6). (Note that in addition to the reaction shown in Scheme 2, HF can also react at the anode to form LiF, according to: $2Li^+ + 2e^- + 2HF \rightarrow 2LiF + H_2$.) Further, low water concentrations are thought to alter the pathway of $LiPF_6$ salt decomposition to produce more $OPF_2(OCH_3)$ (Scheme 2),[69] which again is consistent with our ^{19}F NMR data (Figure 7). In summary, the LFP cathode cycled at low voltages leads to the formation of $OPF_2(OCH_3)$ in solution and relatively low amounts of LiF in the SEI of the anode, which are evidence for small quantities of water and acidic species in the cell, beneficial for SEI stability and Li deposition uniformity, as observed in our *operando* ^{7}Li NMR spectra.

Conversely, the NMC811/Cu cell continues to charge and the dehydrogenation of EC to vinylene carbonate (VC) starts at ~3.8 V,[72] as detected in *in situ* ^{1}H solution NMR (Figure S16). Additional H^+ from dehydrogenation leads to an increasingly acidic environment that breaks down PF_6^- into PF_5 and HF (Scheme 2).[49] Given that NMC811 is moisture sensitive and contains higher quantities of Li_2CO_3 during fabrication and storage, we expect that native Li_2CO_3 on the cathode surface will chemically react with HF, producing more water than the LFP cell. The high water

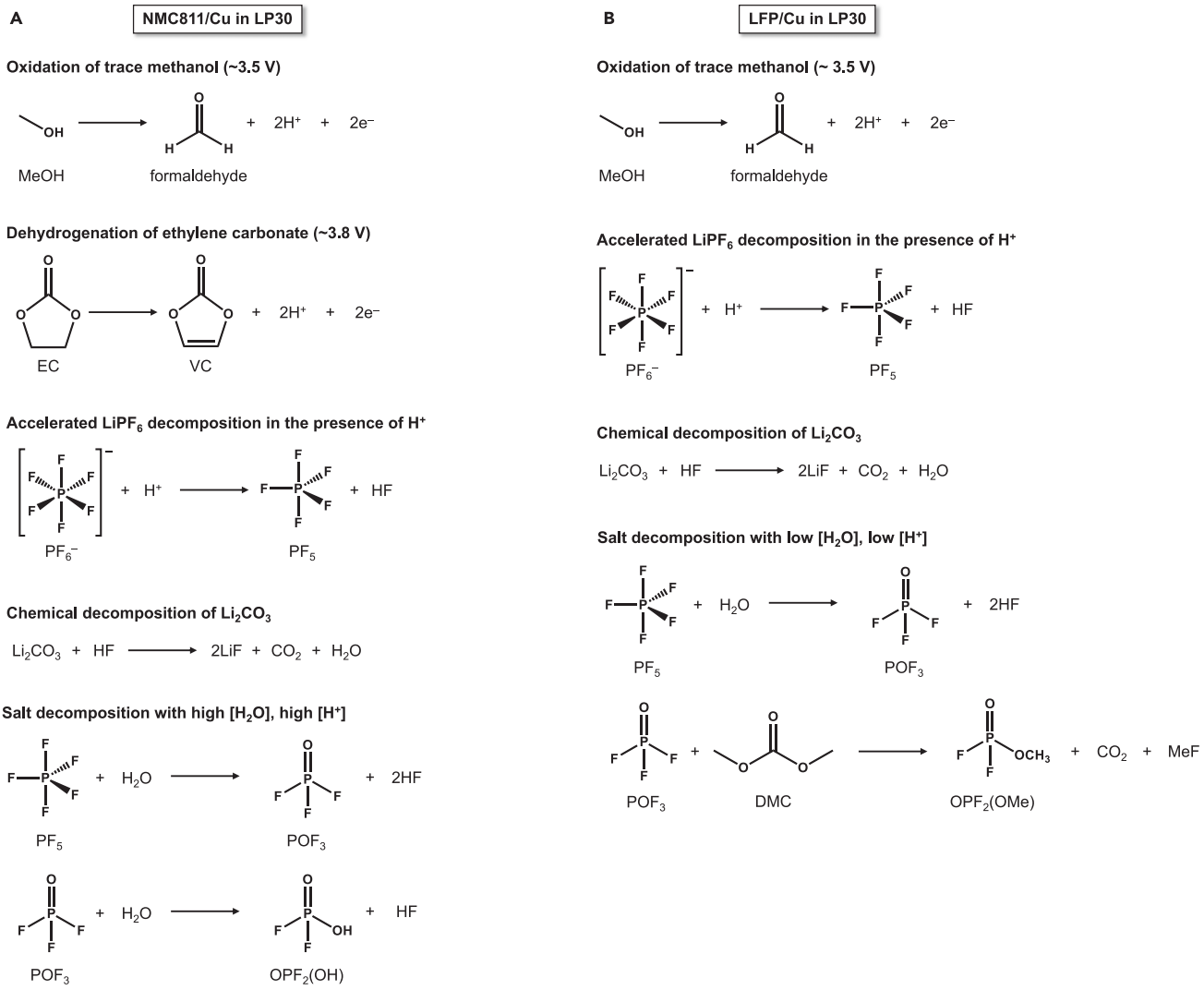

Scheme 2. Proposed (electro)chemical decomposition reactions for NMC/Cu and LFP/Cu cells during electrochemical cycling

Electrochemical and chemical decomposition reactions that occur during cycling of (A) NMC811/Cu and (B) LFP/Cu batteries in LP30. Trace impurities in LFP/Cu cells lead to small quantities of H_2O and H^+ in LFP/Cu cells and the formation of $OPF_2(OMe)$ in ^{19}F NMR and lower amounts of LiF in XPS. Higher concentrations of water and HF in NMC811/Cu cells produce more LiF and predominately $OPF_2O_2^-$ breakdown products in XPS and ^{19}F NMR, respectively.

concentration will drive the formation of $OPF_2(OH)$ and HF over $OPF_2(OCH_3)$,[69] which is supported by our ^{19}F NMR (Figure 7). In general, increased cell voltage will lead to more electrolyte decomposition and more acidic species in the NMC811/Cu battery. Increased H^+/HF can electrochemically or chemically produce more LiF on the Li metal anode and may explain the higher quantities of LiF seen in XPS (Figure 6). Alterations in electrolyte decomposition pathways at different operating potentials modulate the SEI on Li metal as well as the Cu current collector and, in turn, influence Li electrodeposition/dissolution. Using a NMC811 cathode will increase the concentration of acidic species, such as HF, POF_3, and PF_5, which can directly attack the SEI[43] on Li metal and/or drive transition metal dissolution and SEI disruption.[47,50,73–75] Analysis of the Li metal electrodes with XPS did not detect transition metals embedded in the SEI, and electron paramagnetic resonance spectroscopy (EPR) did not show any dissolved Mn^{2+} after ten cycles. However, we note

that these metals may simply be below the limit of detection at such low cycle numbers. Either way, the concentration of the acidic components (and their byproducts) that damage the Li SEI is significantly lower when we use LFP and, thus, we see less dead Li^0 and more reversible Li plating/stripping, even when using a conventional carbonate electrolyte, as seen by our *operando* ^{7}Li NMR (Figures 3 and 4).

Given that cathode selection will vary based on end application, the way in which we design and operate Li metal batteries must reflect how the negative electrode reacts to cathode potential. For example, when pairing Li metal with a high-voltage Ni-rich cathode, we see that electrolyte oxidation reactions correlate with the formation of modest surface area (mossy) deposits that evolve into high surface area Li filaments. The initial porous Li deposits, combined with the acidic species produced from EC oxidation, prove to be detrimental to the cell. Previous work by Betz et al.[45] studied Li deposition morphologies produced by LFP, NMC622, and $LiNi_{0.5}Mn_{1.5}O_4$ (LNMO), and saw that increased Mn content (which likely cause issues from HF-driven dissolution and implantation in the anode SEI) in batteries induced Li plating structures that are more likely to grow through the separator and cause short circuiting. SEM images of these Li deposits are visually consistent with those we see generated from our batteries that contain NMC811. Because these structures are correlated with increased salt breakdown, we suggest that Li metal batteries that use NMC811 need to prevent the formation of HF, either through tuning the salt composition, salt concentration, or solvent choice in the electrolyte to reduce or remove HF and/or mitigate dehydrogenation of EC.[76–78] Overwhelming evidence in the literature supports the notion that cathode coatings and electrolyte additives improve the performance of Li/NMC811 batteries,[79–87] but if these electrolytes still generate HF, these systems may have inherent limitations over time (e.g., surfaces can also etch, sacrificial additives deplete, etc.). Another route to prevent the formation of dead Li^0 buildup in NMC811 batteries may be the use of electrochemical protocols that preferentially strip from the tip of Li microstructures rather than the root.[88] Comparison of our electrochemical cycling data across different stack pressures for NMC811 vs. LFP additionally suggests that if we minimize the surface area of the Li deposit, the reversibility between the two cell types begins to converge (e.g., Li^0 cyclability in NMC811/Cu cells is quite stochastic at low stack pressures but improves at 1 MPa; Tables S1, S2, and S5). However, without modifying the electrolyte to prevent HF generation, benefits will be limited to early cell life,[89] and the fact that the LFP cells can reach higher and more consistent CE values at lower stack pressures still makes them more desirable for practical applications.

When a Li metal anode is created from LFP, Li metal losses are mostly parasitic or corrosive in nature. In principle, the lower operating voltage of LFP should make it easier to focus on optimizing the electrolyte to enable reversible Li stripping/plating and prevent corrosion at the Li/Cu interfaces. For low-cost applications that use LFP, electrolytes that passivate Li metal and are stable to high carbon contents in the cathode would be suitable.[90–92] Another aspect to consider with high CE batteries is that once nearly all of the Li is removed from the current collector, more Li/Cu interfaces will be exposed (and likely covered by a very thin SEI), so Cu surface treatments[54,93,94] will become more important to minimize corrosion.

Conclusions

In summary, we identified key differences in electrolyte degradation pathways, Li plating morphology, and modes of Li inventory loss between anode-free Li metal batteries that use either NMC811 or LFP as the cathode. Through three-electrode cycling measurements, we demonstrated that NMC811/Cu cells have evolving Li

nucleation/stripping overpotentials and transport limitations at the Cu counter electrode, whereas LFP/Cu cells show consistent and reversible cycling. *Operando* ^{7}Li NMR spectroscopy further underscored the difference in Li plating behavior between the two cell types. We noninvasively detect the growth of high surface area Li deposits, accompanied by a deleterious accumulation of dead Li^0 in NMC811/Cu cells, while LFP/Cu cells show higher CE through denser Li deposition. The buildup of dead Li^0 and SEI at the surface of the anode in NMC811/Cu batteries was determined to be the root cause of increasing cell polarization during repeated plating and stripping. This undesirable behavior at the anode is related to decomposition of the electrolyte and instabilities in the SEI that arise due to the higher operating voltage (4.2 V) of NMC811 compared to LFP. ^{19}F NMR spectroscopy and XPS data confirm that acidic electrolyte degradation species, notably HF from water in the electrolyte that is generated during cycling, exacerbate salt decomposition and SEI destabilization. Because LFP/Cu cells have a lower operating voltage, they may be more amenable to electrolyte and substrate optimization protocols developed for Li/Li. To harness the potential of high-voltage cathodes like NMC811, on the other hand, oxidative processes that produce protons at the cathode must be taken into consideration, even though they often involve well-known SEI-formers that benefit the anode, like EC.

EXPERIMENTAL PROCEDURES

Resource availability

Lead contact

Further information and requests for resources and materials should be directed to and will be fulfilled by the lead contact, Lauren Marbella (lem2221@columbia.edu).

Materials availability

This study did not generate new unique reagents.

Data and code availability

- All data reported in this paper will be shared by the lead contact upon request.
- All original code has been deposited at Open Science Framework: https://osf.io/mr26b/ and is publicly available as of the date of publication.
- Any additional information required to reanalyze the data reported in this paper is available from the lead contact upon request.

Materials

Prismatically wound, anode-free, dry pouch cells with a capacity of 200 mAh, containing either $LiNi_{0.8}Co_{0.1}Mn_{0.1}O_2$ (NMC811) or $LiFePO_4$ (LFP) cathode, were purchased from Li-FUN Technology (Zhuzhou, Hunan Province, China). These NMC811 cathodes have a formula of active materials (AMs): conductive carbon: binder = 96.4%: 1.6%: 2.0 %, and the LFP cathodes have 96.7%: 1.5%: 1.8%. The NMC811 and LFP cathodes are reported to be synthesized at a press density of 3.3 and 2.4 g/cc, with a coating areal mass loading of 14.72 and 16.55 mg/cm^2, respectively. Three-electrode (3E) coin cell casings were purchased from Arbin Instruments (College Station, Texas, USA). 3.65-mm o.d. FEP (fluorinated ethylene polypropylene copolymer) NMR tube liners used for *in situ* solution NMR measurements were purchased from Wilmad LabGlass. For *operando* NMR measurements, the polyether ether ketone (PEEK) plastic cell capsules were provided by ePROBE GmbH (Erfurt, Germany). For measuring the internal stack pressure inside these cells, Fujifilm Prescale Tactile Pressure Indicating Sensor Film was purchased from Sensor Products Inc. (Madison, New Jersey, USA). 1 M Li hexafluorophosphate ($LiPF_6$) in 1:1 ethylene carbonate:dimethyl carbonate (EC:DMC 1:1, v/v, LP30,

battery grade) and dimethyl carbonate (DMC, anhydrous, >99%) were used as received from Sigma Aldrich.

Electrochemistry

Li-FUN pouch cells filled with LP30 electrolyte were prepared in an Ar-filled glovebox (O_2 < 0.1 ppm, H_2O < 0.5 ppm). Pouch cells were filled with 600 μL of electrolyte, vacuum sealed, and soaked overnight before electrochemical cycling. Galvanostatic cycling was performed at a C-rate of C/2 based on stack capacity, between 2.5–3.65 V LFP/Cu cells and 3.0–4.2 V for NMC811/Cu cells. For comparison with the *operando* NMR multilayer cells, we used a hydraulic cylinder (CHDKGB40-25) from SMC Pneumatics to apply stack pressures of 0.3 MPa or 1 MPa to the pouch cells during cycling. All cells were cycled in ambient temperature.

Electrochemical tests were also conducted on 3E coin cells. These special 3E coin cell casings resemble a typical 2032 coin cell, except that the top casing contains an electronically isolated stainless steel circular "island" in the center, measuring about 5 mm o.d., onto which a reference electrode disk is placed. On the outside of the coin cell, this stainless-steel island protrudes out from the top casing such that it can be electronically connected to the potentiostat using a special 3E coin cell holder (we used Arbin's 3E coin cell holder with the Arbin MSTAT cycler). The bottom casing (containing a gasket) is identical to that of a typical 2032 coin cell. For cell assembly, we first pressed a 3-mm o.d. Li disc onto the reference electrode lead on the top casing. A 7-mm o.d. Celgard disc was then pressed onto this Li disc. Next, a Cu electrode measuring 12.7 mm o.d., with a 5-mm i.d. concentric hole cut out, was placed on top of the stack. By using a Celgard disc smaller in diameter than the Cu disk, the Cu makes contact easily with the coin cell casing. Next, a 15-mm o.d. glass fiber separator was placed onto the stack, and 200 μL of LP30 electrolyte was added. A 12.7-mm o.d. cathode (NMC811 or LFP), followed by a 0.75-mm-thick spacer, a stainless-steel spring, and the bottom coin cell casing were then placed onto the stack, in that order. The cell was crimped using a hydraulic crimper fitted with a 3E die (Arbin Instruments). All components (cathode, anode films) were extracted from as-purchased Li-FUN pouch cells. 3E cells were rested at OCV for 48 h and then cycled at a rate of C/3 for 10 cycles (3–4.2 V for NMC811 cells and 2.5–3.65 V for LFP cells). The capacities of these cells were calculated by scaling the 200-mAh capacity of Li-FUN pouch cells by the areal ratio between punched-out electrodes for the coin cell and the total cathode area in each pouch cell. We assumed that only the inside surface of the double-sided cathode would contribute to the cell capacity when reconstructed into coin cells. Control experiments indicate that similar polarization and capacity fade is observed for the batteries when using single-sided electrodes, indicating that differences in capacity loss are likely due to pressure in the coin cell. The Arbin cycler measures V_{cell} ($V_{cathode}$ vs. V_{anode}) and $V_{cathode}$ ($V_{working}$ vs. V_{ref}). V_{anode} ($V_{counter}$ vs. V_{ref}) were obtained via the formula $V_{anode} = V_{cathode} - V_{cell}$.

Operando ^{7}Li NMR spectroscopy

In order to assemble plastic capsule cells for *operando* ^{7}Li NMR, the cathode, anode (i.e., Cu current collector), and separator extracted from dry Li-FUN pouch cells outside of the glovebox. The electrodes and separator were cut into 4 × 11 cm strips and reassembled in a prismatic winding configuration. The resulting cells were smaller and exhibited capacities of approximately 25 mAh. Once assembled into a multilayer, the cell stack was dried in 60°C *in vacuo* for 24 h, then brought inside of the glovebox to be soaked in excess electrolyte for another 24 h. After soaking, it was placed in the PEEK plastic cell capsule and ~100 μL of additional electrolyte

was added prior to sealing. The holes that allow the electrical leads to come out of the capsule were sealed with a rubber O-ring and Permatex 5-Minute Epoxy. The internal stack pressure of the plastic capsule cells was measured by a pressure-sensitive paper to be approximately 0.8 MPa. Additionally, we compare the performance of the NMR cells to as-received pouch cells at different stack pressures (Table S5) and, based on these data, believe it lies between 0.3 and 1 MPa. Galvanostatic cycling was performed at an approximate C-rate of ~C/2 based on stack capacity, between 2.5–3.65 V LFP/Cu cells and 3.0–4.2 V for NMC811/Cu cells.

Prior work shows that *operando* NMR can be used to study degradation in materials harvested from industrial-scale electric vehicle batteries in two-electrode plastic pouch cells.[95] Separate work demonstrated that a three-electrode configuration can be used to boost the signal-to-noise ratio of *operando* NMR spectroscopy as well as perform *operando* cyclic voltammetry during the NMR experiment.[96] These works suggest that NMR can be used to (1) study thick electrodes and (2) add additional current collector to the cell while remaining quantitative. Our approach to performing quantitative NMR in the presence of multiple layers of electrodes is discussed in the results and the supplemental information, when we determine the precise mode of Li loss in the cells.

All *operando* NMR experiments were performed on a Bruker 400 Avance NEO spectrometer equipped with an automatic tuning matching cycler (ATMC) *in situ* NMR probe (ePROBE GmbH) using an 11-mm i.d. Ag-coated Cu solenoidal coil with 5 MHz low-pass filters to reduce interference between the circuit for electrochemistry and the magnetic field. Galvanostatic cycling was controlled by connecting the probe to a Biologic SP-150 potentiostat. Each one-dimensional (1D) NMR spectrum was collected at room temperature using a recycle delay (d1) of 1 s (>5 × T_1 for Li metal) and 512 scans, resulting in an experimental time of about 8 min per spectrum. ^{7}Li chemical shifts were externally referenced to LP30 at 0 ppm and the 90° radiofrequency (rf) pulse width was 7.4 μs. Spectra were manually phased and automatically baseline corrected in Bruker Topspin software (version 4.1.4). Further data processing, such as peak integration, additional baseline correction, and plotting, was done via a Python program, which uses the package nmrglue[97] to import and process data, as well as some additional in-house processing and plotting functionalities. Additional details on spectral processing and quantification are described in the supplemental information.

Scanning electron microscopy

SEM images of the Cu current collector after Li plating were collected using a Zeiss Sigma VP Schottky Thermal Field emission SEM with a Gemini objective lens. Before imaging, all samples were washed twice in 1 mL of DMC for 3 s each to remove residual salts and dried overnight *in vacuo* to prevent solvent evaporation in the SEM chamber and charging under the electron beam. Each sample was cut into smaller pieces to be mounted onto an Al stub in the glovebox using carbon tape, then transferred into the SEM chamber using an airtight jar, minimizing exposure to ambient atmosphere to <10 s.

X-ray photoelectron spectroscopy

Cycled anodes were extracted from cells in the glovebox and washed twice in 1 mL of DMC for 3 s each. These samples were then dried *in vacuo* overnight to remove residual solvent. Pristine uncycled copper samples were not washed. The samples were mounted onto an airtight portable transfer vessel inside the glovebox, after which the vessel was then taken out of the glovebox and carried to the City University

of New York Advanced Science Research Center (CUNY ASRC), where it could be brought into the PHI Versaprobe II X-ray photoelectron spectroscope, all without exposing the samples to air. Chamber pressure was <1.0 × 10^{-8} Torr, and XPS spectra were collected with a hemispherical analyzer and an Al X-ray source. CasaXPS was used to fit spectra; the adventitious carbon peak in the C 1s spectrum of each sample was referenced to 284.8 eV.

In situ solution NMR spectroscopy

In situ solution NMR spectroscopy measurements were conducted by assembling and cycling a battery cell in an NMR tube, as described and shown in detail in a previous work by our group.[50] In brief, the cell contains a cathode (NMC811 or LFP), a Cu anode, and a LP30 electrolyte (300 μL) assembled in a 3.65-mm o.d. FEP NMR tube liner (dried at 60°C overnight prior to use). The tube cell is submerged into a 5-mm o.d. glass NMR tube containing 0.1 mL of DMSO-d_6 (for locking and shimming) and secured in place with Teflon tape, allowing us to collect high-resolution ^{1}H and ^{19}F NMR spectra during electrochemical cycling. Electrodes were placed into the tube approximately 25-mm from the bottom of the FEP liner, where they are completely submerged in the electrolyte. The cathode used in the *operando* experiments is a 20- × 2.5-mm-wide rectangular film cast onto Al foil (10 mm in length of excess of the film was inserted into heat-shrink chemically resistant electrical insulation tubing containing a 22-cm-long pure Cu wire, whereby upon heat-treating the tubing, the shrinkage electrically connects the Cu anode to the electrode within the tubing). A 20- × 2.5-mm piece of Cu film (6 μm thick) was used as the anode, which was rinsed in acetone and dried prior to use. Like the cathode, the Cu anode was also connected to a 22-cm-long Cu wire via heat-shrink insulation. The heat-shrink tubing prevented cell shorting along the length of the NMR tube. The Cu anode was wrapped in a single layer of Celgard 2325 separator (dried at 60°C for 24 h prior to use). The AM loading was estimated such that the first cycle was consistent with C/10 cycling (∼2–3 mg), which was 50 μA for the LFP cells and 65 μA for the NMC811 cells. The voltage limits were 2.5–3.65 V for the LFP cells and 3.0–4.2 V for the NMC811 cells.

NMC811/LFP cathode films used in these *in situ* NMR cells were prepared in-house from a slurry of 8:1:1 Active material (AM):C45 Carbon:Polyvinylidene Fluoride (PVDF). AM and C45 were first hand-ground in a mortar and pestle for 10 min. This mixture was then added to a solution of the PVDF binder in NMP to create a viscous slurry. The slurry was then cast onto an Al current collector (25 μm thick, MTI Corporation) using a 150-μm doctor blade and dried at 100°C under vacuum overnight. Once dried, cathode films were stored in an Ar-filled glovebox to minimize exposure to air and moisture. Typical mass loadings of AM per cathode were 4–9 mg cm^{-2}.

SUPPLEMENTAL INFORMATION

Supplemental information can be found online at https://doi.org/10.1016/j.chempr.2024.06.008.

ACKNOWLEDGMENTS

This work was supported, in part, by National Science Foundation (NSF) CAREER award (CBET-2045262). A portion of this work was supported by the Research Corporation for Science Advancement through a Cottrell Scholar award (28206). J.C.H. was supported by the NSF Graduate Research Fellowship Program (NSF GRFP no. 2021278071). K.R.M.C. was supported by the NSF through the Columbia University

Materials Research and Engineering Center (MRSEC) on Precision-Assembled Quantum Materials Research Experiences for Undergraduates (REU) Program (DMR-2011738). We thank Dr. Tai-De Li for assistance with running the XPS measurements at the CUNY ASRC and Prof. Dan Steingart for access to the vacuum sealer for pouch cells. We also thank Dr. Richard May for helpful discussions on experimental setup and Dr. Svetlana Menkin and Jana Fritzke at the University of Cambridge for additional fruitful discussions.

AUTHOR CONTRIBUTIONS

Y.K. and L.E.M. conceived of the study. Y.K. and A.S.-A. designed and carried out *operando* NMR experiments; K.R.M.C. helped make *operando* NMR battery samples. J.C.H. performed *in situ* solution NMR experiments and three-electrode cycling measurements. Y.K. performed electrochemical testing of pouch and *operando* cells and prepared and analyzed samples with SEM and XPS. P.J.B.B. prepared figures and analyzed electrochemical cycling data. Y.K. and A.S.-A. prepared figures for the manuscript and analyzed and interpreted NMR data in conjunction with P.L., O.P., and L.E.M.; Y.K. and L.E.M. wrote and edited the first draft of the manuscript. All authors commented and edited subsequent and final drafts.

DECLARATION OF INTERESTS

The authors declare no competing interests.

Received: December 2, 2023
Revised: March 19, 2024
Accepted: June 5, 2024
Published: July 2, 2024

REFERENCES

1. Deng, J., Bae, C., Denlinger, A., and Miller, T. (2020). Electric Vehicles Batteries: Requirements and Challenges. Joule *4*, 511–515. https://doi.org/10.1016/j.joule.2020.01.013.

2. Duan, J., Tang, X., Dai, H., Yang, Y., Wu, W., Wei, X., and Huang, Y. (2020). Building Safe Lithium-Ion Batteries for Electric Vehicles: A Review. Electrochem. Energ. Rev. *3*, 1–42. https://doi.org/10.1007/s41918-019-00060-4.

3. Çabukoglu, E., Georges, G., Küng, L., Pareschi, G., and Boulouchos, K. (2018). Battery electric propulsion: An option for heavy-duty vehicles? Results from a Swiss case-study. Transp. Res. C *88*, 107–123. https://doi.org/10.1016/j.trc.2018.01.013.

4. Forrest, K., Mac Kinnon, M., Tarroja, B., and Samuelsen, S. (2020). Estimating the technical feasibility of fuel cell and battery electric vehicles for the medium and heavy duty sectors in California. Appl. Energy *276*, 115439. https://doi.org/10.1016/j.apenergy.2020.115439.

5. Cunanan, C., Tran, M.-K., Lee, Y., Kwok, S., Leung, V., and Fowler, M. (2021). A Review of Heavy-Duty Vehicle Powertrain Technologies: Diesel Engine Vehicles, Battery Electric Vehicles, and Hydrogen Fuel Cell Electric Vehicles. Clean. Technol. *3*, 474–489. https://doi.org/10.3390/cleantechnol3020028.

6. Damiano, A., Porru, M., Salimbeni, A., Serpi, A., Castiglia, V., Di Tommaso, A.O., Miceli, R., and Schettino, G. (2018). Batteries for Aerospace: a Brief Review. In AEIT International Annual Conference, pp. 1–6. https://doi.org/10.23919/AEIT.2018.8577355.

7. Boukoberine, M.N., Zhou, Z., and Benbouzid, M. (2019). Power Supply Architectures for Drones - A Review. In IECON 2019 - 45th Annual Conference of the IEEE Industrial Electronics Society, pp. 5826–5831. https://doi.org/10.1109/IECON.2019.8927702.

8. Louli, A.J., Eldesoky, A., Weber, R., Genovese, M., Coon, M., deGooyer, J., Deng, Z., White, R.T., Lee, J., Rodgers, T., et al. (2020). Diagnosing and correcting anode-free cell failure via electrolyte and morphological analysis. Nat. Energy *5*, 693–702. https://doi.org/10.1038/s41560-020-0668-8.

9. Niu, C., Liu, D., Lochala, J.A., Anderson, C.S., Cao, X., Gross, M.E., Xu, W., Zhang, J.-G., Whittingham, M.S., Xiao, J., and Liu, J. (2021). Balancing interfacial reactions to achieve long cycle life in high-energy lithium metal batteries. Nat. Energy *6*, 723–732. https://doi.org/10.1038/s41560-021-00852-3.

10. Qian, J., Adams, B.D., Zheng, J., Xu, W., Henderson, W.A., Wang, J., Bowden, M.E., Xu, S., Hu, J., and Zhang, J.-G. (2016). Anode-Free Rechargeable Lithium Metal Batteries. Adv. Funct. Materials *26*, 7094–7102. https://doi.org/10.1002/adfm.201602353.

11. Xiao, J., Li, Q., Bi, Y., Cai, M., Dunn, B., Glossmann, T., Liu, J., Osaka, T., Sugiura, R., Wu, B., et al. (2020). Understanding and applying coulombic efficiency in lithium metal batteries. Nat. Energy *5*, 561–568. https://doi.org/10.1038/s41560-020-0648-z.

12. Zhang, R., Shen, X., Zhang, Y.-T., Zhong, X.-L., Ju, H.-T., Huang, T.-X., Chen, X., Zhang, J.-D., and Huang, J.-Q. (2022). Dead lithium formation in lithium metal batteries: A phase field model. J. Energy Chem. *71*, 29–35. https://doi.org/10.1016/j.jechem.2021.12.020.

13. Chen, K.-H., Wood, K.N., Kazyak, E., LePage, W.S., Davis, A.L., Sanchez, A.J., and Dasgupta, N.P. (2017). Dead lithium: mass transport effects on voltage, capacity, and failure of lithium metal anodes. J. Mater. Chem. A *5*, 11671–11681. https://doi.org/10.1039/C7TA00371D.

14. Sanchez, A.J., Kazyak, E., Chen, Y., Chen, K.-H., Pattison, E.R., and Dasgupta, N.P. (2020). Plan-View Operando Video Microscopy of Li Metal Anodes: Identifying the Coupled Relationships among Nucleation, Morphology, and Reversibility. ACS Energy Lett. *5*, 994–1004. https://doi.org/10.1021/acsenergylett.0c00215.

15. Bai, P., Li, J., Brushett, F.R., and Bazant, M.Z. (2016). Transition of lithium growth mechanisms in liquid electrolytes. Energy Environ. Sci. *9*, 3221–3229. https://doi.org/10.1039/C6EE01674J.

16. Zhang, Y., Zuo, T.-T., Popovic, J., Lim, K., Yin, Y.-X., Maier, J., and Guo, Y.-G. (2020). Towards better Li metal anodes: Challenges and strategies. Mater. Today *33*, 56–74. https://doi.org/10.1016/j.mattod.2019.09.018.

17. Liu, D.-H., Bai, Z., Li, M., Yu, A., Luo, D., Liu, W., Yang, L., Lu, J., Amine, K., and Chen, Z. (2020). Developing high safety Li-metal anodes for future high-energy Li-metal batteries: strategies and perspectives. Chem. Soc. Rev. *49*, 5407–5445. https://doi.org/10.1039/C9CS00636B.

18. Li, Z., Huang, J., Yann Liaw, B., Metzler, V., and Zhang, J. (2014). A review of lithium deposition in lithium-ion and lithium metal secondary batteries. J. Power Sources *254*, 168–182. https://doi.org/10.1016/j.jpowsour.2013.12.099.

19. Liu, J., Bao, Z., Cui, Y., Dufek, E.J., Goodenough, J.B., Khalifah, P., Li, Q., Liaw, B.Y., Liu, P., Manthiram, A., et al. (2019). Pathways for practical high-energy long-cycling lithium metal batteries. Nat. Energy *4*, 180–186. https://doi.org/10.1038/s41560-019-0338-x.

20. Horstmann, B., Shi, J., Amine, R., Werres, M., He, X., Jia, H., Hausen, F., Cekic-Laskovic, I., Wiemers-Meyer, S., Lopez, J., et al. (2021). Strategies towards enabling lithium metal in batteries: interphases and electrodes. Energy Environ. Sci. *14*, 5289–5314. https://doi.org/10.1039/D1EE00767J.

21. Lin, D., Liu, Y., and Cui, Y. (2017). Reviving the lithium metal anode for high-energy batteries. Nat. Nanotechnol. *12*, 194–206. https://doi.org/10.1038/nnano.2017.16.

22. Fang, C., Wang, X., and Meng, Y.S. (2019). Key Issues Hindering a Practical Lithium-Metal Anode. Trends in Chemistry *1*, 152–158. https://doi.org/10.1016/j.trechm.2019.02.015.

23. Hobold, G.M., Lopez, J., Guo, R., Minafra, N., Banerjee, A., Shirley Meng, Y., Shao-Horn, Y., and Gallant, B.M. (2021). Moving beyond 99.9% Coulombic efficiency for lithium anodes in liquid electrolytes. Nat. Energy *6*, 951–960. https://doi.org/10.1038/s41560-021-00910-w.

24. Zeng, Z., Murugesan, V., Han, K.S., Jiang, X., Cao, Y., Xiao, L., Ai, X., Yang, H., Zhang, J.-G., Sushko, M.L., and Liu, J. (2018). Non-flammable electrolytes with high salt-to-solvent ratios for Li-ion and Li-metal batteries. Nat. Energy *3*, 674–681. https://doi.org/10.1038/s41560-018-0196-y.

25. Qiu, F., Li, X., Deng, H., Wang, D., Mu, X., He, P., and Zhou, H. (2019). A Concentrated Ternary-Salts Electrolyte for High Reversible Li Metal Battery with Slight Excess Li. Adv. Energy Mater. *9*, 1803372. https://doi.org/10.1002/aenm.201803372.

26. Suo, L., Xue, W., Gobet, M., Greenbaum, S.G., Wang, C., Chen, Y., Yang, W., Li, Y., and Li, J. (2018). Fluorine-donating electrolytes enable highly reversible 5-V-class Li metal batteries. Proc. Natl. Acad. Sci. USA *115*, 1156–1161. https://doi.org/10.1073/pnas.1712895115.

27. Fan, X., Chen, L., Ji, X., Deng, T., Hou, S., Chen, J., Zheng, J., Wang, F., Jiang, J., Xu, K., and Wang, C. (2018). Highly Fluorinated Interphases Enable High-Voltage Li-Metal Batteries. Chem *4*, 174–185. https://doi.org/10.1016/j.chempr.2017.10.017.

28. Rustomji, C.S., Yang, Y., Kim, T.K., Mac, J., Kim, Y.J., Caldwell, E., Chung, H., and Meng, Y.S. (2017). Liquefied gas electrolytes for electrochemical energy storage devices. Science *356*, eaal4263. https://doi.org/10.1126/science.aal4263.

29. Goodenough, J.B., and Kim, Y. (2010). Challenges for Rechargeable Li Batteries. Chem. Mater. *22*, 587–603. https://doi.org/10.1021/cm901452z.

30. Winter, M., Barnett, B., and Xu, K. (2018). Before Li ion batteries. Chem. Rev. *118*, 11433–11456. https://doi.org/10.1021/acs.chemrev.8b00422.

31. Xu, K. (2023). Electrolytes, Interfaces and Interphases: Fundamentals and Applications in Batteries (Royal Society of Chemistry).

32. Xu, K. (2014). Electrolytes and Interphases in Li-Ion Batteries and Beyond. Chem. Rev. *114*, 11503–11618. https://doi.org/10.1021/cr500003w.

33. Zhang, W., Zhang, S., Fan, L., Gao, L., Kong, X., Li, S., Li, J., Hong, X., and Lu, Y. (2019). Tuning the LUMO Energy of an Organic Interphase to Stabilize Lithium Metal Batteries. ACS Energy Lett. *4*, 644–650. https://doi.org/10.1021/acsenergylett.8b02483.

34. Ren, X., Chen, S., Lee, H., Mei, D., Engelhard, M.H., Burton, S.D., Zhao, W., Zheng, J., Li, Q., Ding, M.S., et al. (2018). Localized High-Concentration Sulfone Electrolytes for High-Efficiency Lithium-Metal Batteries. Chem *4*, 1877–1892. https://doi.org/10.1016/j.chempr.2018.05.002.

35. Peled, E., and Menkin, S. (2017). Review—SEI: Past, Present and Future. J. Electrochem. Soc. *164*, A1703–A1719. https://doi.org/10.1149/2.1441707jes.

36. Li, T., Zhang, X.-Q., Shi, P., and Zhang, Q. (2019). Fluorinated Solid-Electrolyte Interphase in High-Voltage Lithium Metal Batteries. Joule *3*, 2647–2661. https://doi.org/10.1016/j.joule.2019.09.022.

37. Lee, Y., Lee, T.K., Kim, S., Lee, J., Ahn, Y., Kim, K., Ma, H., Park, G., Lee, S.-M., Kwak, S.K., and Choi, N.-S. (2020). Fluorine-incorporated interface enhances cycling stability of lithium metal batteries with Ni-rich NCM cathodes. Nano Energy *67*, 104309. https://doi.org/10.1016/j.nanoen.2019.104309.

38. Cui, C., Yang, C., Eidson, N., Chen, J., Han, F., Chen, L., Luo, C., Wang, P.-F., Fan, X., and Wang, C. (2020). A Highly Reversible, Dendrite-Free Lithium Metal Anode Enabled by a Lithium-Fluoride-Enriched Interphase. Adv. Mater. *32*, e1906427. https://doi.org/10.1002/adma.201906427.

39. Brown, Z.L., Jurng, S., Nguyen, C.C., and Lucht, B.L. (2018). Effect of Fluoroethylene Carbonate Electrolytes on the Nanostructure of the Solid Electrolyte Interphase and Performance of Lithium Metal Anodes. ACS Appl. Energy Mater. *1*, 3057–3062. https://doi.org/10.1021/acsaem.8b00705.

40. Heiskanen, S.K., Kim, J., and Lucht, B.L. (2019). Generation and Evolution of the Solid Electrolyte Interphase of Lithium-Ion Batteries. Joule *3*, 2322–2333. https://doi.org/10.1016/j.joule.2019.08.018.

41. Zheng, G., Xiang, Y., Chen, S., Ganapathy, S., Verhallen, T.W., Liu, M., Zhong, G., Zhu, J., Han, X., Wang, W., et al. (2020). Additives synergy for stable interface formation on rechargeable lithium metal anodes. Energy Storage Mater. *29*, 377–385. https://doi.org/10.1016/j.ensm.2019.12.027.

42. Zhao, Y., Zhou, T., Jeurgens, L.P.H., Kong, X., Choi, J.W., and Coskun, A. (2023). Electrolyte engineering for highly inorganic solid electrolyte interphase in high-performance lithium metal batteries. Chem *9*, 682–697. https://doi.org/10.1016/j.chempr.2022.12.005.

43. Heiskanen, S.K., Laszczynski, N., and Lucht, B.L. (2020). Perspective—Surface Reactions of Electrolyte with LiNixCoyMnzO2 Cathodes for Lithium Ion Batteries. J. Electrochem. Soc. *167*, 100519. https://doi.org/10.1149/1945-7111/ab981c.

44. Solchenbach, S., Hong, G., Freiberg, A.T.S., Jung, R., and Gasteiger, H.A. (2018). Electrolyte and SEI Decomposition Reactions of Transition Metal Ions Investigated by On-Line Electrochemical Mass Spectrometry. J. Electrochem. Soc. *165*, A3304–A3312. https://doi.org/10.1149/2.0511814jes.

45. Betz, J., Brinkmann, J.-P., Nölle, R., Lürenbaum, C., Kolek, M., Stan, M.C., Winter, M., and Placke, T. (2019). Cross Talk between Transition Metal Cathode and Li Metal Anode: Unraveling Its Influence on the Deposition/Dissolution Behavior and Morphology of Lithium. Adv. Energy Mater. *9*, 1900574. https://doi.org/10.1002/aenm.201900574.

46. Louli, A.J., Eldesoky, A., Degooyer, J., Coon, M., Aiken, C.P., Simunovic, Z., Metzger, M., and Dahn, J.R. (2022). Different Positive Electrodes for Anode-Free Lithium Metal Cells. J. Electrochem. Soc. *169*, 040517. https://doi.org/10.1149/1945-7111/ac62c4.

47. Harris, O.C., Lin, Y., Qi, Y., Leung, K., and Tang, M.H. (2020). How Transition Metals Enable Electron Transfer through the SEI: Part I. Experiments and Butler-Volmer Modeling. J. Electrochem. Soc. *167*, 013502. https://doi.org/10.1149/2.0022001JES.

48. Zhang, X.-Q., Wang, X.-M., Li, B.-Q., Shi, P., Huang, J.-Q., Chen, A., and Zhang, Q. (2020). Crosstalk shielding of transition metal ions for long cycling lithium–metal batteries. J. Mater. Chem. A *8*, 4283–4289. https://doi.org/10.1039/C9TA12269A.

49. Hestenes, J.C., and Marbella, L.E. (2023). Beyond Composition: Surface Reactivity and Structural Arrangement of the Cathode–Electrolyte Interphase. ACS Energy Lett. *8*, 4572–4596. https://doi.org/10.1021/acsenergylett.3c01529.

50. Hestenes, J.C., Sadowski, J.T., May, R., and Marbella, L.E. (2023). Transition Metal Dissolution Mechanisms and Impacts on Electronic Conductivity in Composite LiNi0.5Mn1.5O4 Cathode Films. ACS Mater. Au *3*, 88–101. https://doi.org/10.1021/acsmaterialsau.2c00060.

51. Rinkel, B.L.D., Vivek, J.P., Garcia-Araez, N., and Grey, C.P. (2022). Two electrolyte decomposition pathways at nickel-rich cathode

surfaces in lithium-ion batteries. Energy Environ. Sci. *15*, 3416–3438. https://doi.org/10.1039/D1EE04053G.

52. Yu, Y., Karayaylali, P., Katayama, Y., Giordano, L., Gauthier, M., Maglia, F., Jung, R., Lund, I., and Shao-Horn, Y. (2018). Coupled LiPF6 Decomposition and Carbonate Dehydrogenation Enhanced by Highly Covalent Metal Oxides in High-Energy Li-Ion Batteries. J. Phys. Chem. C *122*, 27368–27382. https://doi.org/10.1021/acs.jpcc.8b07848.

53. May, R., Fritzsching, K.J., Livitz, D., Denny, S.R., and Marbella, L.E. (2021). Rapid Interfacial Exchange of Li Ions Dictates High Coulombic Efficiency in Li Metal Anodes. ACS Energy Lett. *6*, 1162–1169. https://doi.org/10.1021/acsenergylett.1c00112.

54. Menkin, S., O'Keefe, C.A., Gunnarsdóttir, A.B., Dey, S., Pesci, F.M., Shen, Z., Aguadero, A., and Grey, C.P. (2021). Toward an Understanding of SEI Formation and Lithium Plating on Copper in Anode-Free Batteries. J. Phys. Chem. C Nanomater. Interfaces *125*, 16719–16732. https://doi.org/10.1021/acs.jpcc.1c03877.

55. Seok, J., Gannett, C.N., Yu, S.-H., and Abruña, H.D. (2021). Understanding the Impacts of Li Stripping Overpotentials at the Counter Electrode by Three-Electrode Coin Cell Measurements. Anal. Chem. *93*, 15459–15467. https://doi.org/10.1021/acs.analchem.1c03422.

56. Bond, T., Gauthier, R., Gasilov, S., and Dahn, J.R. (2022). In-Situ Computed Tomography of Particle Microcracking and Electrode Damage in Cycled NMC622/Graphite Pouch Cell Batteries. J. Electrochem. Soc. *169*, 080531. https://doi.org/10.1149/1945-7111/ac8a22.

57. Bhattacharyya, R., Key, B., Chen, H., Best, A.S., Hollenkamp, A.F., and Grey, C.P. (2010). In situ NMR observation of the formation of metallic lithium microstructures in lithium batteries. Nat. Mater. *9*, 504–510. https://doi.org/10.1038/nmat2764.

58. Chang, H.J., Trease, N.M., Ilott, A.J., Zeng, D., Du, L.-S., Jerschow, A., and Grey, C.P. (2015). Investigating Li Microstructure Formation on Li Anodes for Lithium Batteries by in Situ 6Li/7Li NMR and SEM. J. Phys. Chem. C *119*, 16443–16451. https://doi.org/10.1021/acs.jpcc.5b03396.

59. Gunnarsdóttir, A.B., Amanchukwu, C.V., Menkin, S., and Grey, C.P. (2020). Noninvasive In Situ NMR Study of "Dead Lithium" Formation and Lithium Corrosion in Full-Cell Lithium Metal Batteries. J. Am. Chem. Soc. *142*, 20814–20827. https://doi.org/10.1021/jacs.0c10258.

60. Marbella, L.E., Zekoll, S., Kasemchainan, J., Emge, S.P., Bruce, P.G., and Grey, C.P. (2019). 7Li NMR Chemical Shift Imaging To Detect Microstructural Growth of Lithium in All-Solid-State Batteries. Chem. Mater. *31*, 2762–2769. https://doi.org/10.1021/acs.chemmater.8b04875.

61. Hsieh, Y.-C., Leißing, M., Nowak, S., Hwang, B.-J., Winter, M., and Brunklaus, G. (2020). Quantification of Dead Lithium via In Situ Nuclear Magnetic Resonance Spectroscopy. Cell Reports Physical Science *1*, 100139. https://doi.org/10.1016/j.xcrp.2020.100139.

62. Zhou, L., Leskes, M., Ilott, A.J., Trease, N.M., and Grey, C.P. (2013). Paramagnetic electrodes and bulk magnetic susceptibility effects in the in situ NMR studies of batteries: Application to Li1.08Mn1.92O4 spinels. J. Magn. Reson. *234*, 44–57. https://doi.org/10.1016/j.jmr.2013.05.011.

63. Trease, N.M., Zhou, L., Chang, H.J., Zhu, B.Y., and Grey, C.P. (2012). In situ NMR of lithium ion batteries: Bulk susceptibility effects and practical considerations. Solid State Nucl. Magn. Reson. *42*, 62–70. https://doi.org/10.1016/j.ssnmr.2012.01.004.

64. Mukherjee, P., Paddison, J.A.M., Xu, C., Ruff, Z., Wildes, A.R., Keen, D.A., Smith, R.I., Grey, C.P., and Dutton, S.E. (2021). Sample Dependence of Magnetism in the Next-Generation Cathode Material LiNi0.8Mn0.1Co0.1O2. Inorg. Chem. *60*, 263–271. https://doi.org/10.1021/acs.inorgchem.0c02899.

65. Upreti, S., Chernova, N.A., Xiao, J., Miller, J.K., Yakubovich, O.V., Cabana, J., Grey, C.P., Chevrier, V.L., Ceder, G., Musfeldt, J.L., et al. (2012). Crystal Structure, Physical Properties, and Electrochemistry of Copper Substituted LiFePO4 Single Crystals. Chem. Mater. *24*, 166–173. https://doi.org/10.1021/cm2026619.

66. Walder, B.J., Conradi, M.S., Borchardt, J.J., Merrill, L.C., Sorte, E.G., Deichmann, E.J., Anderson, T.M., Alam, T.M., and Harrison, K.L. (2021). NMR spectroscopy of coin cell batteries with metal casings. Sci. Adv. *7*, eabg8298. https://doi.org/10.1126/sciadv.abg8298.

67. Menkin, S., Fritzke, J.B., Larner, R., de Leeuw, C., Choi, Y., Gunnarsdóttir, A.B., and Grey, C.P. (2024). Insights into soft short circuit-based degradation of lithium metal batteries. Faraday Discuss. *248*, 277–297. https://doi.org/10.1039/D3FD00101F.

68. Kolesnikov, A., Kolek, M., Dohmann, J.F., Horsthemke, F., Börner, M., Bieker, P., Winter, M., and Stan, M.C. (2020). Galvanic Corrosion of Lithium-Powder-Based Electrodes. Adv. Energy Mater. *10*, 2000017. https://doi.org/10.1002/aenm.202000017.

69. Wiemers-Meyer, S., Winter, M., and Nowak, S. (2016). Mechanistic insights into lithium ion battery electrolyte degradation – a quantitative NMR study. Phys. Chem. Chem. Phys. *18*, 26595–26601. https://doi.org/10.1039/C6CP05276B.

70. Stich, M., Göttlinger, M., Kurniawan, M., Schmidt, U., and Bund, A. (2018). Hydrolysis of LiPF6 in Carbonate-Based Electrolytes for Lithium-Ion Batteries and in Aqueous Media. J. Phys. Chem. C *122*, 8836–8842. https://doi.org/10.1021/acs.jpcc.8b02080.

71. Freiberg, A.T.S., Sicklinger, J., Solchenbach, S., and Gasteiger, H.A. (2020). Li2CO3 decomposition in Li-ion batteries induced by the electrochemical oxidation of the electrolyte and of electrolyte impurities. Electrochim. Acta *346*, 136271. https://doi.org/10.1016/j.electacta.2020.136271.

72. Zhang, Y., Katayama, Y., Tatara, R., Giordano, L., Yu, Y., Fraggedakis, D., Sun, J.G., Maglia, F., Jung, R., Bazant, M.Z., et al. (2020). Revealing electrolyte oxidation via carbonate dehydrogenation on Ni-based oxides in Li-ion batteries by in situ Fourier transform infrared spectroscopy. Energy Environ. Sci. *13*, 183–199. https://doi.org/10.1039/C9EE02543J.

73. Lee, Y.K., Park, J., and Lu, W. (2017). A Comprehensive Study of Manganese Deposition and Side Reactions in Li-Ion Battery Electrodes. J. Electrochem. Soc. *164*, A2812–A2822. https://doi.org/10.1149/2.1851712jes.

74. Harris, O.C., Leung, K., and Tang, M.H. (2020). How Transition Metals Enable Electron Transfer through the SEI: Part II. Redox-Cycling Mechanism Model and Experiment. J. Electrochem. Soc. *167*, 013503. https://doi.org/10.1149/2.0032001JES.

75. Wang, C., Xing, L., Vatamanu, J., Chen, Z., Lan, G., Li, W., and Xu, K. (2019). Overlooked electrolyte destabilization by manganese (II) in lithium-ion batteries. Nat. Commun. *10*, 3423. https://doi.org/10.1038/s41467-019-11439-8.

76. Xue, W., Gao, R., Shi, Z., Xiao, X., Zhang, W., Zhang, Y., Zhu, Y.G., Waluyo, I., Li, Y., Hill, M.R., et al. (2021). Stabilizing electrode–electrolyte interfaces to realize high-voltage Li||LiCoO2 batteries by a sulfonamide-based electrolyte. Energy Environ. Sci. *14*, 6030–6040. https://doi.org/10.1039/D1EE01265G.

77. Dose, W.M., Li, W., Temprano, I., O'Keefe, C.A., Mehdi, B.L., De Volder, M.F.L., and Grey, C.P. (2022). Onset Potential for Electrolyte Oxidation and Ni-Rich Cathode Degradation in Lithium-Ion Batteries. ACS Energy Lett. *7*, 3524–3530. https://doi.org/10.1021/acsenergylett.2c01722.

78. Tatara, R., Yu, Y., Karayaylali, P., Chan, A.K., Zhang, Y., Jung, R., Maglia, F., Giordano, L., and Shao-Horn, Y. (2019). Enhanced Cycling Performance of Ni-Rich Positive Electrodes (NMC) in Li-Ion Batteries by Reducing Electrolyte Free-Solvent Activity. ACS Appl. Mater. Interfaces *11*, 34973–34988. https://doi.org/10.1021/acsami.9b11942.

79. Zheng, J., Engelhard, M.H., Mei, D., Jiao, S., Polzin, B.J., Zhang, J.-G., and Xu, W. (2017). Electrolyte additive enabled fast charging and stable cycling lithium metal batteries. Nat. Energy *2*, 1–8. https://doi.org/10.1038/nenergy.2017.12.

80. Zhang, H., Eshetu, G.G., Judez, X., Li, C., Rodriguez-Martínez, L.M., and Armand, M. (2018). Electrolyte Additives for Lithium Metal Anodes and Rechargeable Lithium Metal Batteries: Progress and Perspectives. Angew. Chem. Int. Ed. Engl. *57*, 15002–15027. https://doi.org/10.1002/anie.201712702.

81. Hsieh, Y.-C., Thienenkamp, J.H., Huang, C.-J., Tao, H.-C., Rodehorst, U., Hwang, B.J., Winter, M., and Brunklaus, G. (2021). Revealing the Impact of Film-Forming Electrolyte Additives on Lithium Metal Batteries via Solid-State NMR/MRI Analysis. J. Phys. Chem. C *125*, 252–265. https://doi.org/10.1021/acs.jpcc.0c09771.

82. Zhang, X., Wu, Q., Guan, X., Cao, F., Li, C., and Xu, J. (2020). Lithium dendrite-free and fast-charging for high voltage nickel-rich lithium metal batteries enabled by bifunctional sulfone-containing electrolyte additives. J. Power Sources *452*, 227833. https://doi.org/10.1016/j.jpowsour.2020.227833.

83. Xin, F., Goel, A., Zhou, H., and Whittingham, M.S. (2023). Enabling Long Cycling with

Excellent Structure Stability for High-Nickel Layered Cathodes in Lithium Metal Batteries. ACS Materials Lett. *5*, 1969–1973. https://doi.org/10.1021/acsmaterialslett.3c00301.

84. Sun, X.-G., Jafta, C.J., Tan, S., Borisevich, A., Gupta, R.B., and Paranthaman, M.P. (2022). Facile Surface Coatings for Performance Improvement of NMC811 Battery Cathode Material. J. Electrochem. Soc. *169*, 020565. https://doi.org/10.1149/1945-7111/ac5302.

85. Ahaliabadeh, Z., Miikkulainen, V., Mäntymäki, M., Mousavihashemi, S., Lahtinen, J., Lide, Y., Jiang, H., Mizohata, K., Kankaanpää, T., and Kallio, T. (2021). Understanding the Stabilizing Effects of Nanoscale Metal Oxide and Li–Metal Oxide Coatings on Lithium-Ion Battery Positive Electrode Materials. ACS Appl. Mater. Interfaces *13*, 42773–42790. https://doi.org/10.1021/acsami.1c11165.

86. Herzog, M.J., Gauquelin, N., Esken, D., Verbeeck, J., and Janek, J. (2021). Increased Performance Improvement of Lithium-Ion Batteries by Dry Powder Coating of High-Nickel NMC with Nanostructured Fumed Ternary Lithium Metal Oxides. ACS Appl. Energy Mater. *4*, 8832–8848. https://doi.org/10.1021/acsaem.1c00939.

87. Zhang, X.-Q., Cheng, X.-B., Chen, X., Yan, C., and Zhang, Q. (2017). Fluoroethylene Carbonate Additives to Render Uniform Li Deposits in Lithium Metal Batteries. Adv. Funct. Materials *27*, 1605989. https://doi.org/10.1002/adfm.201605989.

88. Louli, A.J., Coon, M., Genovese, M., deGooyer, J., Eldesoky, A., and Dahn, J.R. (2021). Optimizing Cycling Conditions for Anode-Free Lithium Metal Cells. J. Electrochem. Soc. *168*, 020515. https://doi.org/10.1149/1945-7111/abe089.

89. Fang, C., Lu, B., Pawar, G., Zhang, M., Cheng, D., Chen, S., Ceja, M., Doux, J.-M., Musrock, H., Cai, M., et al. (2021). Pressure-tailored lithium deposition and dissolution in lithium metal batteries. Nat. Energy *6*, 987–994. https://doi.org/10.1038/s41560-021-00917-3.

90. Logan, E.R., Hebecker, H., Eldesoky, A., Luscombe, A., Johnson, M.B., and Dahn, J.R. (2020). Performance and Degradation of LiFePO4/Graphite Cells: The Impact of Water Contamination and an Evaluation of Common Electrolyte Additives. J. Electrochem. Soc. *167*, 130543. https://doi.org/10.1149/1945-7111/abbbbe.

91. Ramasubramanian, B., Sundarrajan, S., Chellappan, V., Reddy, M.V., Ramakrishna, S., and Zaghib, K. (2022). Recent Development in Carbon-LiFePO4 Cathodes for Lithium-Ion Batteries: A Mini Review. Batteries *8*, 133. https://doi.org/10.3390/batteries8100133.

92. Metzger, M., Sicklinger, J., Haering, D., Kavakli, C., Stinner, C., Marino, C., and Gasteiger, H.A. (2015). Carbon Coating Stability on High-Voltage Cathode Materials in H2O-Free and H2O-Containing Electrolyte. J. Electrochem. Soc. *162*, A1227–A1235. https://doi.org/10.1149/2.0461507jes.

93. Shu, J., Shui, M., Huang, F., Xu, D., Ren, Y., Hou, L., Cui, J., and Xu, J. (2011). Comparative study on surface behaviors of copper current collector in electrolyte for lithium-ion batteries. Electrochim. Acta *56*, 3006–3014. https://doi.org/10.1016/j.electacta.2011.01.004.

94. Assegie, A.A., Cheng, J.-H., Kuo, L.-M., Su, W.-N., and Hwang, B.-J. (2018). Polyethylene oxide film coating enhances lithium cycling efficiency of an anode-free lithium-metal battery. Nanoscale *10*, 6125–6138. https://doi.org/10.1039/C7NR09058G.

95. Sanders, K.J., Aguilera, A.R., Keffer, J.R., Balcom, B.J., Halalay, I.C., and Goward, G.R. (2022). Transient lithium metal plating on graphite: Operando 7Li nuclear magnetic resonance investigation of a battery cell using a novel RF probe. Carbon *189*, 377–385. https://doi.org/10.1016/j.carbon.2021.12.082.

96. Lopez, J.L.L., Grandinetti, P.J., and Co, A.C. (2018). Enhancing the real-time detection of phase changes in lithium–graphite intercalated compounds through derivative operando (dOp) NMR cyclic voltammetry. J. Mater. Chem. A *6*, 231–243. https://doi.org/10.1039/C7TA07521A.

97. Helmus, J.J., and Jaroniec, C.P. (2013). Nmrglue: An open source Python package for the analysis of multidimensional NMR data. J. Biomol. NMR *55*, 355–367. https://doi.org/10.1007/S10858-013-9718-X/FIGURES/8.